



A tale of two phase diagrams: Interplay of ordering and hydrogen uptake in Pd–Au–H

J. Magnus Rahm, Joakim Löfgren, Erik Fransson, Paul Erhart*

Chalmers University of Technology, Department of Physics, S-412 96 Gothenburg, Sweden

ARTICLE INFO

Article history:

Received 12 February 2021

Revised 8 April 2021

Accepted 10 April 2021

Available online 17 April 2021

ABSTRACT

Due to their ability to reversibly absorb/desorb hydrogen without hysteresis, Pd–Au nanoalloys have been proposed as materials for hydrogen sensing. For sensing, it is important that absorption/desorption isotherms are reproducible and stable over time. A few studies have pointed to the influence of short and long range chemical order on these isotherms, but many aspects of the impact of chemical order have remained unexplored. Here, we use alloy cluster expansions to describe the thermodynamics of hydrogen in Pd–Au in a wide concentration range. We investigate how different chemical orderings, corresponding to annealing at different temperatures as well as different external pressures of hydrogen, impact the behavior of the material with focus on its hydrogen absorption/desorption isotherms. In particular, we find that a long-range ordered $L1_2$ phase is expected to form if the H_2 pressure is sufficiently high. Furthermore, we construct the phase diagram at temperatures from 250 K to 500 K, showing that if full equilibrium is reached in the presence of hydrogen, phase separation can often be expected to occur, in stark contrast to the phase diagram in para-equilibrium. Our results explain the experimental observation that absorption/desorption isotherms in Pd–Au are often stable over time, but also reveal pitfalls for when this may not be the case.

© 2021 The Author(s). Published by Elsevier Ltd on behalf of Acta Materialia Inc. This is an open access article under the CC BY license (<http://creativecommons.org/licenses/by/4.0/>)

1. Introduction

The prospect of hydrogen as a replacement for fossil fuels continues to generate interest in metallic hydrides. Some metals are of particular interest in this context as they can be reversibly loaded and unloaded with hydrogen by tuning the partial pressure of H_2 gas in the environment; Pd is one such example. When loaded with hydrogen, the Pd hydride has a hydrogen density that is orders of magnitudes larger than H_2 gas under the same conditions, and it is therefore a candidate for storing hydrogen [1]. Another potential application of Pd hydrides is sensing [2,3]. Pd nanoparticles that are exposed to hydrogen quickly form a hydride [4], and when doing so, their optical properties change. This change can be easily detected, and Pd nanoparticles can thus be used as reversible hydrogen sensors [5,6]. The use of Pd for hydrogen sensing applications has, however, a major disadvantage; Pd hydride formation at room temperature is associated with a first-order phase transition from a hydrogen-poor α phase to a hydrogen-rich β phase, which causes the sensor response to be a highly non-linear function of H_2 pressure. Since the phase transition is also associ-

ated with hysteresis [7–9], the response moreover differs between the loading and unloading half-cycles. These aspects are generally unfavorable for sensing applications.

Fortunately, these drawbacks can be alleviated by alloying Pd with Au. With around 20 mol-% of Au in Pd, the system can be loaded continuously with hydrogen [10,11], eventually making the sensor readout an almost linear function of H_2 pressure [12–15]. The introduction of another chemical species thus fundamentally changes the thermodynamics of the material and improves its properties. From a scientific as well as practical standpoint, however, an alloy is significantly more complex than a pure metal, and multiple important questions arise: what is the optimal composition, how are the chemical elements ordered under different circumstances, and how does this ordering influence the properties of the material? The influence of overall composition can usually be relatively easily optimized by experimental screening. The chemical ordering, on the other hand, is difficult to both control and measure experimentally, and can be expected to be influenced by conditions during and after fabrication. Moreover, although Pd–Au nanoalloy sensors tend to be stable over time [16], changes may occur over long time-scales due to slow kinetics, which makes the effects tedious to experimentally assess, while they may still be detrimental to the material. Although the study of hydrogen in

* Corresponding author.

E-mail address: erhart@chalmers.se (P. Erhart).

Pd and its alloys has a long and rich history [7,17–23], many fundamental aspects of the Pd–Au–H system are still unknown, and to fully exploit this material it is of paramount importance that its thermodynamics are understood, as it determines the driving forces that underpin the evolution of the atomic scale structure over time.

A few previous studies have successfully used combinations of density-functional theory (DFT) calculations and statistical methods to predict properties of hydrogen in Pd–Au. For example, Mamatkulov and Zhdanov [24] recently developed a model based on DFT calculations that successfully predicted absorption isotherms, highlighting that once octahedral sites without surrounding Au atoms become few, the phase transition and its associated hysteresis disappears. These calculations assumed a Pd–Au lattice with random configuration, which remained unaffected by insertion of hydrogen. This metastable equilibrium, with equilibrium only on the hydrogen sublattice, is commonly referred to as para-equilibrium [25–27]. If the metal atoms are allowed to rearrange in response to hydrogen such that full equilibrium is reached, a significantly more complex phase diagram can be expected [28]. This was indicated experimentally by Lee *et al.* [29], who found that long-range order (LRO) was formed in Pd–Au with 19% Au when subjected to a high pressure of H₂ at high temperatures. Importantly, alloys with this LRO had strikingly different pressure–composition isotherms than those that had not been treated in a high-pressure H₂ gas and lacked LRO. A similar conclusion was reached by Chandrasekhar and Sholl *et al.* [30], who computed hydrogen solubility as a function of chemical order at Au contents 4% and 15%. These results show that the different degrees of equilibration matter for the properties of the Pd–Au–H system, and since many applications depend on reproducible pressure–composition isotherms, chemical order should not be ignored. In this light, it is obvious that a full accounting of the impact of chemical order on the thermodynamics of Pd–Au–H is desirable.

Here, we make a detailed atomic scale study of the thermodynamics of hydrogen in Pd–Au. To this end, we use alloy cluster expansion fitted to DFT to describe the energetics of the system ranging from 0% to 50% Au in Pd and in the full range from no hydrogen to full hydrogen occupation. This approach, which has been successfully applied to similar materials in the past [30–34], allows for very fast evaluation of the energy of a system with hundreds of atoms with an accuracy approaching that of DFT. Using Monte Carlo (MC) simulations, we can elucidate the thermodynamics and, in particular, study how chemical order evolves under different circumstances.

2. Methodology

Our methodology comprises the following steps: (1) we calculate energies of Pd–Au–H structures with different composition and configuration [35,36] with DFT [37–40], (2) fit alloy cluster expansion to these energies [41], and (3) sample the system using MC simulations in different ensembles using the ICET software [36]. The details of these methods are provided in Supplementary Note 1–3. With this methodology, we can extract temperature-dependent thermodynamic quantities with a high accuracy.

In Pd–Au–H, hydrogen primarily occupies octahedral interstitial sites in the face-centered cubic (FCC) lattice formed by Pd–Au (although in some configurations, tetrahedral site may be preferred [24,42]). The full system can thus be viewed as a rock salt structure, i.e., two interpenetrating FCC sublattices, one occupied by Pd and Au, and the other populated with H and vacancies. In the following, we will state concentrations *per sublattice*, such that, for example, the H concentration is 100% if all sites on the H/vacancy sublattice are occupied by H, whereas energies are stated per formula unit (f.u.) with a f.u. being two sites, one per sublattice.

We restricted our training data (and simulations) to Au concentration below 50%, and excluded training data with too large relaxation relative to the reference lattice (as detailed in Supplementary Note 2).

To be able to quantify the uncertainty stemming from the fitting of the cluster expansion (CE) model, we used a Bayesian approach to construct 10 additional CE models [43,44], below referred to as “sampled cluster expansion”. The results below were, however, obtained with the average CE model unless stated otherwise.

In this work, we exploit the possibility to sample the two sublattices with different strategies in the same MC simulation. Specifically, we used different combinations of the canonical, semi-grand canonical (SGC), and variance-constrained semi-grand canonical (VCSGC) [45,46] ensembles. MC simulations in the canonical ensemble involve swapping the chemical identity of two randomly chosen sites on the same sublattice, whereas SGC and VCSGC simulations only involve flipping the chemical identity of one site at a time. The overall composition is thus preserved in the canonical ensemble but not in the SGC or VCSGC ensemble. The canonical ensembles is thus closely related to closed systems (which is usually the case for the Pd–Au sublattice experimentally), whereas the SGC and VCSGC ensemble mimic open systems (which is almost always the case for the H–vacancy sublattice). The SGC and VCSGC ensembles also yield access to the free energy derivative $\partial F/\partial c$, and by extension the partial pressure of H₂, as discussed in Supplementary Note 4. By integration, the free energy landscape can be mapped out and phase diagrams constructed, as detailed in Supplementary Note 6.

3. Results and discussion

3.1. Cluster expansion construction

The CE constructed in this work has a root mean square error for the mixing energies of 8.3meV/f.u. over the training set and of 15.3meV/f.u. over the test set. To put these number in perspective, it is instructive to compare them to the wide span (–100 to 500meV/f.u.) of mixing energies in this system (Fig. 1). The largest errors are frequently found among structures with a large content of Au, which partially explains the large difference in error between training and test set, as the latter contained a higher proportion of structures with high Au content. The predicted energy of all structures (including structures that relaxed too far relative to the reference structure (see Fig. S2) but excluding those with $c_{\text{Au}} > 0.5$) has a good albeit not perfect correlation with the corresponding DFT energies (Fig. 1a, $R^2 = 0.934$). The energies of structures with long relaxation distances are sometimes severely overestimated. This is unsurprising since they were not included in the training data and cannot be expected to be well described by the CE in any case. Many of the poorly described structures are those with higher mixing energies in a series of configurations with the same composition (Fig. 1b–g), and hence are in general less relevant for the thermodynamics of the system.

The effective cluster interactions (ECIs) of the constructed CE exhibit physically sound behavior in the sense that the strongest interactions are those that occur at a short distance, and triplet interactions are generally smaller than pair interactions (Fig. 2). Based on the ECIs, we can already at this point anticipate roughly how the system will behave. The strongest interaction is the one between Au/Pd and its nearest neighbor H/vacancy. We can anticipate that H will be attracted to Pd and vacancies to Au. H–H interactions, on the other hand, are comparatively weak, whereas the positive, short-ranged Au/Pd–Au/Pd ECI indicate that the formation of Pd–Au pairs is energetically favorable.

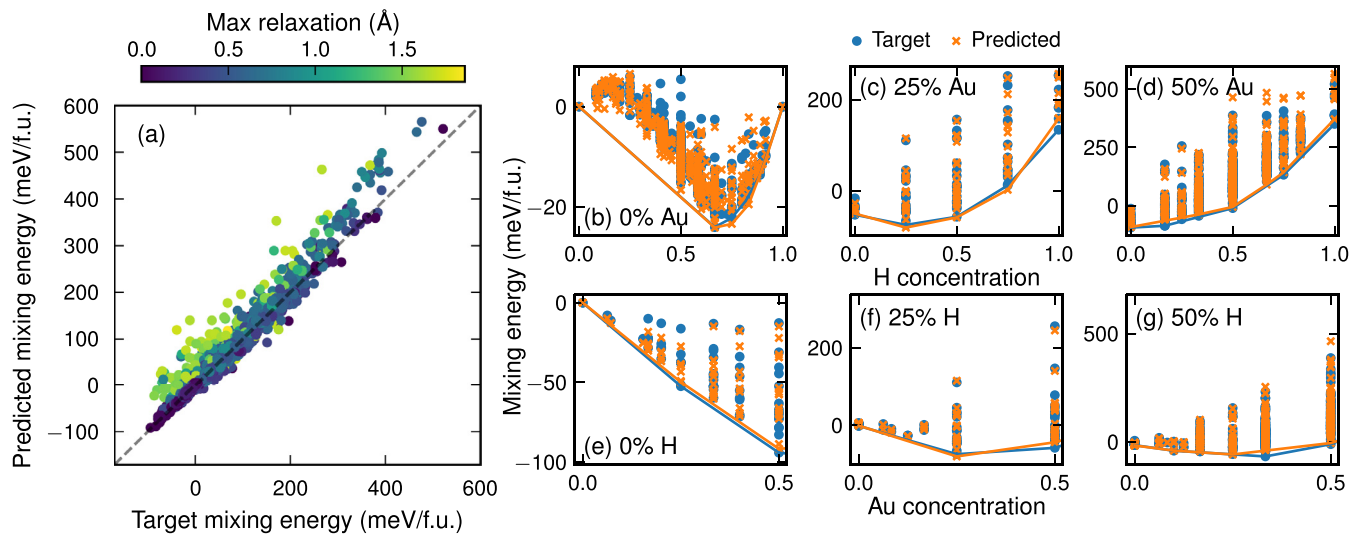


Fig. 1. Mixing energies as predicted with the CE developed in this work compared to target energies from DFT calculations. Structures for which the largest relaxation distance was small (dark blue dots in (a)) are generally well reproduced by the CE, whereas the energy of structures with large relaxation distances are overestimated by the CE (yellow dots in (a)). Only structures with maximum relaxation distance less than 0.5Å were included when training the CE. Mixing energies as a function of H concentration at fixed Au concentration (b–d) and as a function of Au concentration at fixed H concentration (e–g) reveal that the general energy landscape is well reproduced in the concentration intervals considered here.

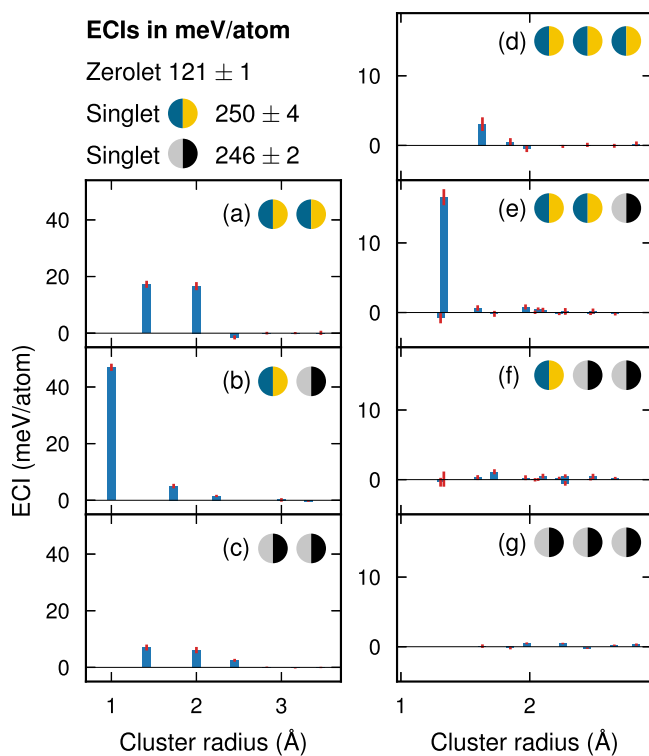


Fig. 2. Effective cluster interactions (ECIs) in the cluster expansion developed in this study, as function of the radius of the cluster, here defined as the average distance between the atoms in the cluster and their center of mass (assuming all atoms have the same mass). Pair ECIs are split in three categories, interactions between Au/Pd and Au/Pd (a), between Au/Pd and H/vacancy (b), and between H/vacancy and H/vacancy (c). In the same vein, triplet interactions are split into four categories depending on the sublattices involved (d)–(g). Error bars, defined as two standard deviations over a set of 100 randomly sampled cluster expansions, are shown in red at the tip of each bar.

3.2. Ordered phases in hydrogen-free Pd–Au

Although the focus of our work is on the thermodynamics of hydrogen in Pd–Au, we begin our analysis with the Pd–Au alloy in absence of hydrogen as ordering on this sublattice turns out to

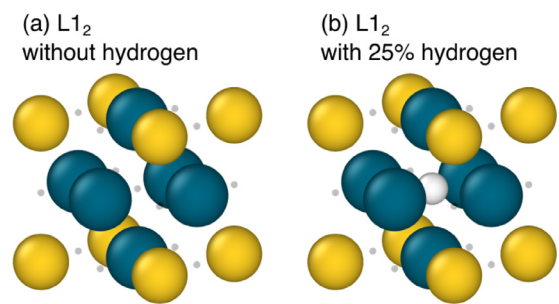


Fig. 3. The L₁₂ phase without hydrogen (a) and with 25% hydrogen (b). Palladium, gold, and hydrogen are shown in blue, yellow, and white, respectively, whereas vacancies are shown as grey dots. In this ordered phase, hydrogen preferentially occupies the site surrounded by nearest neighbor Pd atoms. Note that this choice of cell does not give an accurate representation of compositions; the structures have (a) 25% Au and 75% Pd and (b) the same composition on the Pd–Au sublattice and 25% hydrogen and 75% vacancies on the other.

be also relevant with regard to the hydrogenated system, as discussed below. As our CE is only fitted to structures with 50% Au or less, we restrict our analysis to this composition interval. The mixing energies of structures with 12 Pd/Au atoms or less are negative, meaning mixing is favorable (Fig. 1e). It is, however, still possible that phase separation occurs between ordered (intermetallic) phases. LRO in Pd–Au has been reported in experiments on thin films [47,48] and nanoparticles [49], but has generally not been found in the bulk, suggesting that the energetics causing ordering is either enhanced by surface stress or has critical temperatures too low for ordering to occur readily in bulk samples. By enumerating structures with up to 12 atoms in the cell, our CE identifies three structures on the convex hull between 0 and 50% Au: the trivial case of pure Pd, AuPd₃ in the L₁₂ configuration (Fig. 3a) and AuPd in the L₁₀ configuration. These findings are largely consistent with other computational studies, although other structures have occasionally been found on the convex hull [50,51].

To investigate at below which temperature the L₁₂ phase will appear, we ran MC simulations in the canonical ensemble, i.e., with the composition fixed at 25% Au in Pd, and tracked the LRO parameter (see Supplementary Note 5) as a function of temperature. The

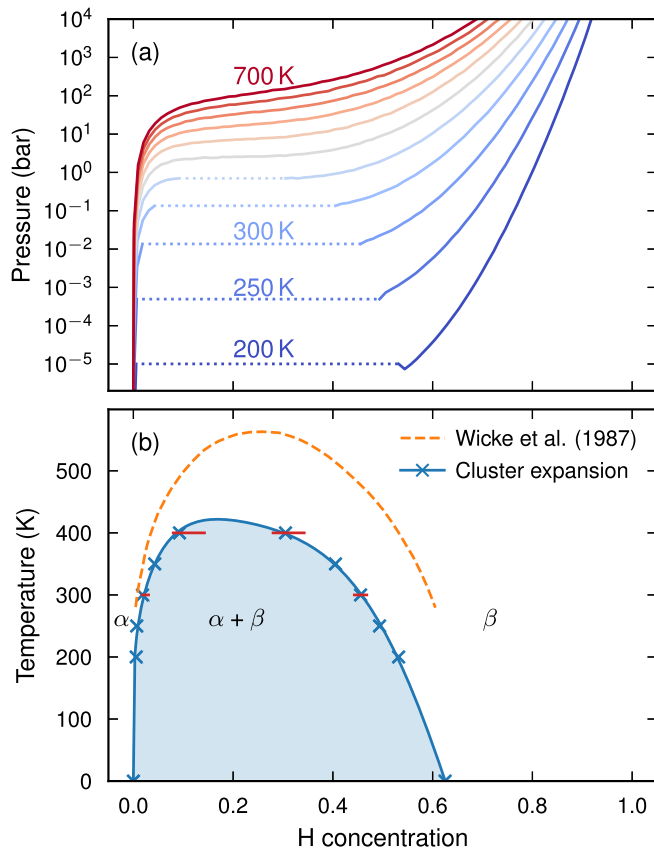


Fig. 4. Pressure–composition isotherms in steps of 50 K for pure Pd hydrides (a). Phase transitions from the hydrogen-poor α phase to the hydrogen-rich β phase have been drawn with a dashed line. These dashed lines indicate the phase boundaries of the two-phase region (blue crosses in (b), blue line is a fit to guide the eye). Compared to experimental results [52] (orange line in (b)), the critical temperature is underestimated, but the uncertainty from the choice of CE is significant, as indicated by the spread of the miscibility gap at 300 and 400 K from ten sampled CEs (red lines indicate difference between minimum and maximum value predicted by these ten CEs). Here, we have disregarded ordered phases with hydrogen concentrations above 0.67, all of which have critical temperatures below 200 K.

results revealed a critical temperatures at 180 K (Fig. S6), with a span among the sampled cluster expansion from less than 150 K to 260 K.

3.3. Hydrogen in pure Pd

We are now ready to add hydrogen to the system. Since the pure Pd hydride (no Au) has been more thoroughly studied than the alloy hydride, we begin in this limit. We carried out VCSGC-MC simulations on the H/vacancy lattice with temperatures between 200 K and 700 K in steps of 50 K. The thus obtained isotherms (Fig. 4a) indicate a low solubility of H in Pd until a “threshold pressure” has been reached. For sufficiently low temperatures, there is then a phase transition from a hydrogen-poor α phase to a hydrogen-rich β phase, which can be detected by integrating the free energy derivative and identify the regions where the free energy curve lies above its convex hull (as outlined in Supplementary Note 6). The corresponding phase diagram is largely consistent with the experimental phase diagram constructed by Wicke and Blaurock [52] (Fig. 4b). The critical temperature, which is challenging to estimate accurately both experimentally and by means of MC simulations, differs approximately 140 K (560 K experimentally and 420 K based on our CE). Although this is a fairly large discrepancy, it should be noted that small variations in the ECIs

have a large impact on the critical temperature; at temperatures close to the critical temperature, uncertainties in the phase boundary become large (quantified by ten sampled cluster expansion; the spread from these ten cluster expansion is indicated with red horizontal bars in Fig. 4b). Discrepancies between simulation and experiment are thus not unexpected, especially given that it is also challenging to construct the phase diagram experimentally.

3.4. Hydrogen loading of fixed Pd–Au lattice: random and para-equilibrium

We are now ready to include Au in the MC simulations. To this end, we note that the two sublattices are markedly different from a kinetic perspective. Hydrogen diffuses easily even at low temperatures, while Pd and Au diffuse over a much longer timescale. To reach full equilibrium, in which the Pd and Au atoms rearrange in response to a change in hydrogen environment, a very slow experiment with H_2 pressure kept constant over extended periods of time, is required (see Sect. 4 below). If the H_2 pressure is more quickly increased/decreased, we may instead assume that the Pd–Au sublattice is frozen and that a metastable equilibrium is reached by rearrangement of the hydrogen atoms only. The chemical order on the Pd–Au sublattice would then typically be dictated by the conditions during fabrication of the alloy, which usually involve a form of thermal annealing. Here, we distinguish two extremes of such a metastable equilibrium: *para-equilibrium*, in which the Pd–Au ordering is equilibrated at 300 K in the absence of H_2 , and *random equilibrium*, in which the Pd–Au lattice is randomized, corresponding to quenching of the system after equilibration at a very high temperature in absence of H_2 .

We can model these situations by only carrying out VCSGC-MC flips on the H/vacancy sublattice. For the random equilibrium, we commence from a simulation cell in which the Pd and Au atoms have been randomly distributed, whereas for para-equilibrium, we run a canonical MC simulation with only Pd and Au and randomly pick a configuration as the fixed Pd–Au lattice. To suppress spurious effects from the particular choice of Pd–Au lattice, we averaged our results over five instances of both cases.

These MC simulations reveal weak short-range order (SRO) (Fig. 5, for definitions see Supplementary Note 5). We first note that the equilibration of the Pd–Au lattice in absence of hydrogen yields a weak propensity for the system to form unlike (Pd–Au) nearest neighbor bonds, whereas bonds that are alike (Au–Au and Pd–Pd) are weakly favored among next-nearest neighbors (Fig. 5a; in random Pd–Au the corresponding order parameters are zero by construction). For nearest neighbor Pd/Au–H/vacancy pairs (Fig. 5b–c), the SRO parameter is negative, indicating that H is more likely to occupy sites next to Pd than next to Au. This confirms what has been observed both with Mössbauer spectroscopy [53] and first-principles calculations [24], namely that it is energetically unfavorable for hydrogen to occupy the sites closest to a Au atom. For next-nearest Pd/Au–H/vacancy neighbors (Fig. 5d–e), on the other hand, the effect is reversed, albeit weaker. The change of sign between first and second nearest-neighbor was observed also by Sonwane *et al.* [54] in a model based on DFT calculations. It is furthermore consistent with the common argument that chemistry causes repulsion between neighboring Au and H, whereas dilation of the lattice by a Au atom gives rise to a more long-ranged elastic attraction [20].

The most pronounced difference between the two types of equilibria is found for the most short-ranged H/vacancy pair (Fig. 5f–g), for which the system in para-equilibrium has a stronger tendency to form H–H pairs. For next-nearest neighbor H/vacancy pairs (Fig. 5h–i) a more complex behavior emerges, with the sign of the SRO parameter being dependent on both H and Au concentration. For high H and Pd content, the SRO parameter is negative,

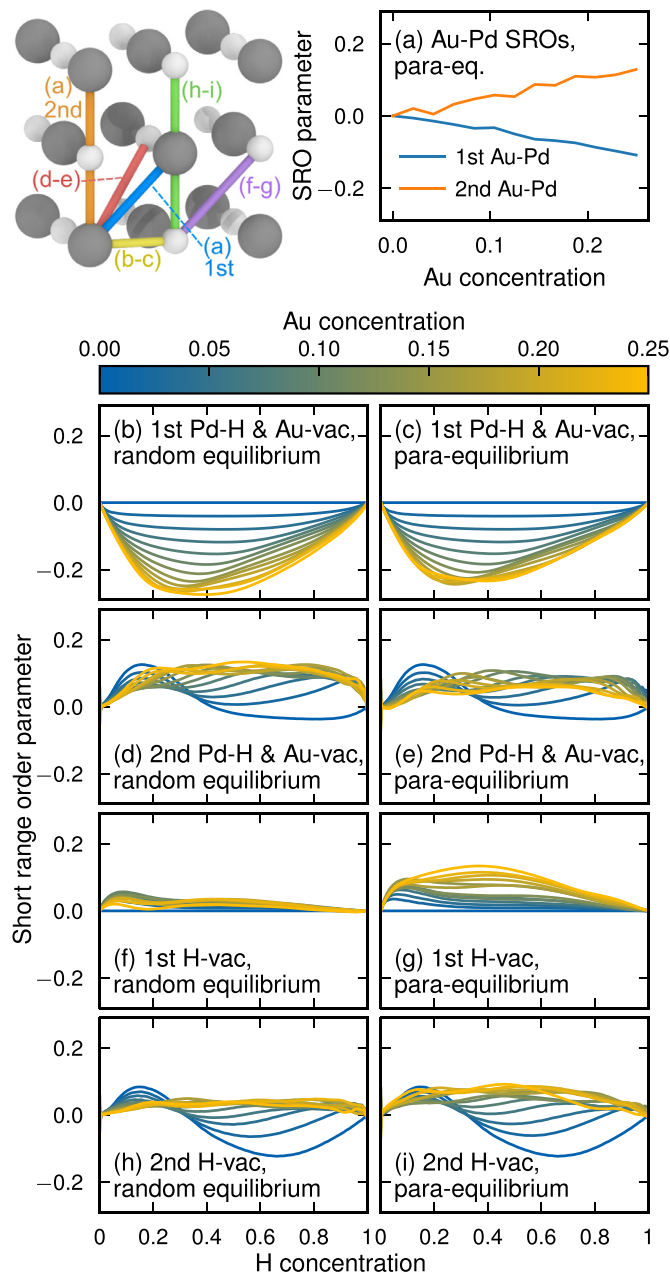


Fig. 5. SRO at 300 K in Pd-Au-H with the Pd-Au lattice fixed in a random configuration (left column) and as equilibrated in absence of H (para-equilibrium, right column). The SRO in the nearest-neighbor shell between the Pd/Au and the H/vacancy lattices (a–b) is negative, which, with our definitions (see Supplementary Note 5), means that H tends to sit close to Pd and vacancies close to Au. In the second Au/Pd shell (c–d), a weak reverse trend is seen throughout most of the H concentration range. In the first H/vacancy shell (f–g), H–H pairs are favored, only weakly in random equilibrium but stronger in para-equilibrium. The behavior is more complex in the second H/vacancy shell, with ordering tendencies being dependent on both H and Au concentrations.

indicating that H atoms are distributed throughout the material, as H–H pairs are not favored. With a high content of Au and/or low content of H, the opposite behavior occurs, i.e., there is a slight excess of H–H pairs. This effect is somewhat more pronounced in para-equilibrium.

Given the quantitative difference in chemical ordering between random Au–Pd and para-equilibrium, we may now look for consequences for their respective thermodynamics. It turns out, however, that their H₂ pressure–composition isotherms (Fig. 6a–b) are

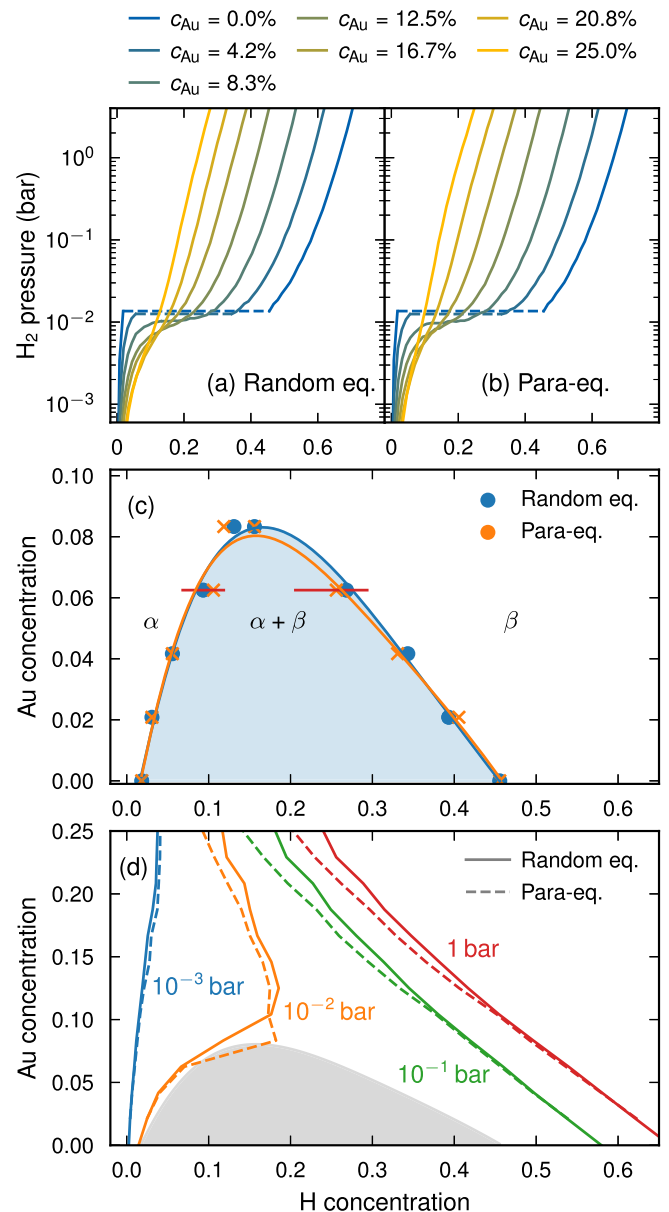


Fig. 6. Pressure–composition isotherms at 300 K for Pd–Au–H with (a) a random Pd–Au sublattice and (b) in para-equilibrium, i.e., with the Pd–Au lattice equilibrated at 300 K in absence of H. Phase transitions from the H-poor α phase to the H-rich β phase are indicated with a dashed line. The corresponding two phase diagrams (c) are almost identical, with the two-phase region closing at approximately 8–9% Au. Red lines at 6.3% Au indicate the range of values obtained from ten sampled CEs. By studying the hydrogen uptake at fixed H₂ pressure as a function of Au concentration (d), it is clear that differences between random and para-equilibrium are found primarily at high H₂ pressures, where at the same pressure the random system absorbs a slightly larger amount of hydrogen than the system in para-equilibrium. Larger variations are also seen at 10^{−2} bar (orange line), since this is close to the plateau pressure. The phase diagram in para-equilibrium is indicated with transparent grey in (d).

very similar. It is only at fairly high Au concentrations, approaching 25% Au, that the isotherms of random and para-equilibrium exhibit discernible differences. At high Au concentrations and high H₂ pressures, the hydrogen uptake is slightly higher in random equilibrium than in para-equilibrium (Fig. 6d). Although this difference is small, there seems to be a weak but consistent trend; when SRO emerges due to lower annealing temperature, the hydrogen uptake at 300 K goes down at pressures above approximately 10 mbar (Fig. S7). The difference seems to be the largest

at a hydrogen pressure around 1 bar, where the fully random alloy with 25% Au absorbs almost 4 percentage points more hydrogen than the one equilibrated in 300 K. These results seem to be in agreement with Chandrasekhar and Sholl [30]. To summarize, the SRO that emerges at low temperatures in Pd–Au makes the material absorb slightly less hydrogen at high H_2 pressures.

The discontinuity in the Au-poor isotherms, which is the hallmark of the phase transition from α to β , disappears quickly when the Au content is increased and it does so in almost exactly the same way for random and para-equilibrium. Consequently, the respective phase diagrams are essentially identical (Fig. 6c). Our results predict a critical Au concentration for the $\alpha + \beta$ two-phase region around 8–9%. This is significantly lower than experimental measurements, which yield estimates that vary from 10–15% (at 303 K) [11] to around 17% (at 298 K) [10]. The prediction of the solvus line is, however, sensitive to small variations in the ECIs (quantified by the spread obtained by sampling ten cluster expansion and indicated by red horizontal bars in Fig. 6c). Thus both our prediction and the experimental value are associated with significant uncertainties.

3.5. Hydrogen loading in full equilibrium

We may now ask what will happen if we allow the Pd–Au lattice to rearrange as we expose it to hydrogen. This situation is commonly referred to as full (or complete) equilibrium. It should be noted that this is an idealization that is very time-consuming to achieve in practice, as in most experiments the H_2 pressure is not maintained long enough to allow for Pd and Au to diffuse to a sufficient extent. Yet, it is important as it provides the thermodynamic driving force for the changes that do occur, although they may only rarely take the system to full equilibrium. To investigate the full equilibrium, we carried out MC simulations in the VCSGC ensemble on both sublattices. Subsequently we obtained the free energy by integration across the concentration plane using many different integration paths, and sampled the convex hull based on these different integration paths (for details, see Supplementary Note 6). Thereby we obtained a heat map of the probability that certain compositions are on the convex hull, which can be interpreted as (an isothermal cut of) the phase diagram (Fig. 7; see Fig. S10 for data at 250 and 500 K). The two-phase region at low Au content observed in para and random equilibrium is present in the full phase diagram at 300 K as well, but is accompanied by a much larger multi-phase region at higher Au concentrations (Fig. 7a). At 400 K, the former two-phase region is almost gone, but the multi-phase region at higher Au contents is still present. This new multi-phase region that appears in the full phase diagram, as opposed to random and para-equilibrium, is largely driven by a particularly stable composition interval around 25% Au and approximately 10–30% H, where at 300 K isobars ranging from 10^{-3} bar to 10^2 bar all converge. A closer look at this composition interval reveals that LRO develops here (Fig. S9). Specifically, the Pd–Au sublattice orders in the $L1_2$ phase, in which the atoms are arranged such that 25% of the hydrogen sites are octahedral “cages” with only Pd nearest neighbors (Fig. 3b). As has been previously reported [24] and can be expected from the ECIs (Fig. 2), occupation of hydrogen at such sites is energetically particularly favorable, and renders this long-range ordered phase particularly stable. At 500 K (Fig. S10b), LRO no longer forms and the phase diagram is largely featureless, i.e., a solid solution can be expected at any concentration (except possibly at high Au content and extremely high H_2 pressures).

The phase diagram in Fig. 7a thus predicts that if a Pd–Au alloy at 300 K with, say, approximately 15% Au is subjected to a H_2 pressure between approximately 10^{-3} bar and 10^2 bar, phase separation will occur. Of the resulting two phases, one will be the $L1_2$ phase with between 10 and 30% H. The character of the other phase de-

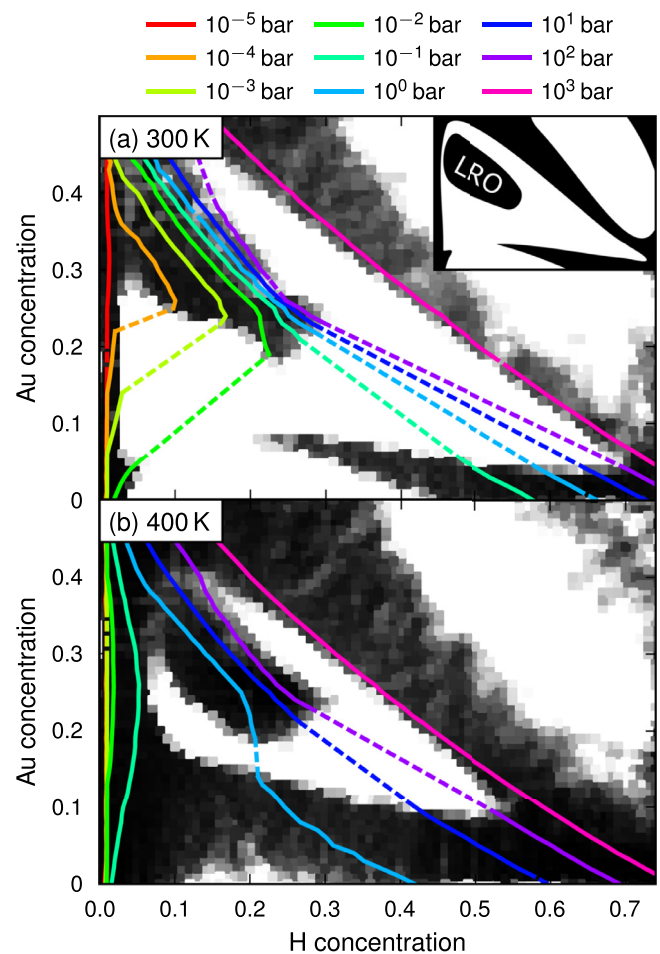


Fig. 7. Phase diagram of hydrogenated Pd–Au in full equilibrium at (a) 300 K and (b) 400 K. Black areas indicate single-phase regions, whereas white areas are multi-phase regions. Isobars (lines of fixed H_2 partial pressure) are drawn with colored lines. Many of the isobars converge in a region around 25% Au and 25% H, where the system exhibits LRO. The remaining dark areas represent a solid solution. The inset shows a schematic representation of the phase diagram to aid its interpretation.

pends on the H_2 pressure; if the pressure is below 10^{-2} bar, the second phase will be the dilute α phase (with Au content strongly dependent on H_2 pressure) whereas if the pressure is above approximately 10^{-2} bar, the second phase will be the hydrogen-rich β phase with approximately 5% Au.

The existence of a long-range ordered phase in hydrogen-treated Pd–Au has been reported experimentally by Lee *et al.* [29], who observed a super-lattice phase in Pd–Au with 19% Au. The structure of this phase could not be determined but the authors reported it to be more complex than $L1_2$. It should perhaps not be ruled out, however, that the off-stoichiometric composition as well as defects such as anti-phase boundaries, which occurred frequently in some of our simulations, may have played a role in these experiments. Importantly, these experiments provide us with an approximate time scale for the transformation between ordered and disordered phases. Specifically, “diagnostic” hydrogen-loading isotherms indicate that at 523 K changes in order take place gradually over many hours [29].

Another region of interest in Fig. 7 is the single-phase region that the 10^3 bar isobar traces out (pink line in Fig. 7). Here, the SRO parameter for nearest neighbor Pd–Au pairs switches sign, indicating a transition from an excess of Pd–Au pairs to an excess of Au–Au and Pd–Pd pairs (Fig. S8). Inspection of the MC trajectories at these composition reveals that the system has started to cluster

into hydrogen-poor Au clusters and hydrogen-rich Pd clusters, both only a few atoms large. Our model considers this phase thermodynamically stable and *not* merely a first step towards full phase separation. It seems plausible that a phase like this may provide a favorable balance between the short-ranged repulsion between Au and H and the long-ranged elastic attraction caused by dilation of the Pd lattice by adjacent Au clusters. It is not surprising that this phase has not been reported experimentally given the very high H_2 pressure required for it to form ($\gtrsim 10^3$ bar). It should be noted that the pressure specified in this region is highly approximate, as this is outside the applicability range of the ideal gas law.

3.6. Impact of annealing conditions on hydrogen solubility

Although full equilibrium will usually not be reached in the time frame of a typical hydrogen loading experiment, there may be circumstances in which full equilibrium is approached. For example, annealing of Pd–Au is sometimes done in the presence of hydrogen in order to prevent oxidation. Although the pressure of H_2 is then typically too low to have a significant impact, the phase diagram Fig. 7 shows that complex behavior may emerge in the presence of hydrogen, especially if the temperature is not too high. We may consider a fairly typical situation in which the alloy is annealed at a particular temperature and H_2 pressure, after which hydrogen absorption/desorption isotherms are measured at another temperature. Since the latter absorption/desorption is usually carried out at a much lower temperature than the annealing, and during a much shorter period of time, it is reasonable to assume that the Pd–Au sublattice gets frozen in during annealing and does not change when measuring the isotherm. The chemical ordering on the Pd–Au sublattice would then be determined entirely by the conditions during annealing.

We now mimic such an experiment by simulating isotherms at 300 K in Pd–Au with 25% of Au annealed in different conditions. To this end, we first run MC simulations at a specified annealing temperature with canonical MC swaps on the Pd–Au sublattice, and SGC MC flips on the H–vacancy sublattice, using a chemical potential corresponding to a fixed H_2 pressure. We then pick five random snapshots from the resulting trajectory, remove the hydrogen, fix the Pd–Au sublattice, and run MC simulations at 300 K with SGC flips on the H–vacancy sublattice only, using a wide range of hydrogen chemical potentials.

Inspection of 300 K isotherms with Pd–Au annealed in 400 K (Fig. 8a) reveals that the hydrogen concentration depends strongly on the conditions during annealing. When annealed in pressures of 10^{-1} bar or lower (blue and orange lines), the isotherms behave as in the random or para-equilibrium case, with an almost linear isotherm (when plotted on a logarithmic scale). For higher pressures, however, the isotherms are markedly different. After annealing in 1, 10 or 100 bar, the uptake of hydrogen at low pressures is much higher, after which the concentration of hydrogen stays at about 25% up to very high pressures, meaning that at sufficiently high pressures, the hydrogen content is in fact higher in Pd–Au samples that were annealed in the absence of hydrogen. The difference between these two kinds of isotherms is that annealing in 1–100 bar induces L_{12} LRO. If the H_2 pressure is raised to 1,000 bar, the ordered phase no longer forms, and the isotherm (brown line in Fig. 8a) becomes more similar to the low-pressure isotherms, although the hydrogen uptake is significantly higher if the H_2 pressure is above a few millibar.

The ordered L_{12} phase is thus clearly distinguishable from the ones lacking LRO already from the isotherms. These findings are consistent with Lee *et al.* [29]. When annealing in 600 K, on the other hand, the temperature is too high for any LRO to emerge, and the 600 K isotherms are essentially identical regardless of annealing pressure (Fig. 8b). It is expected that much higher pressures

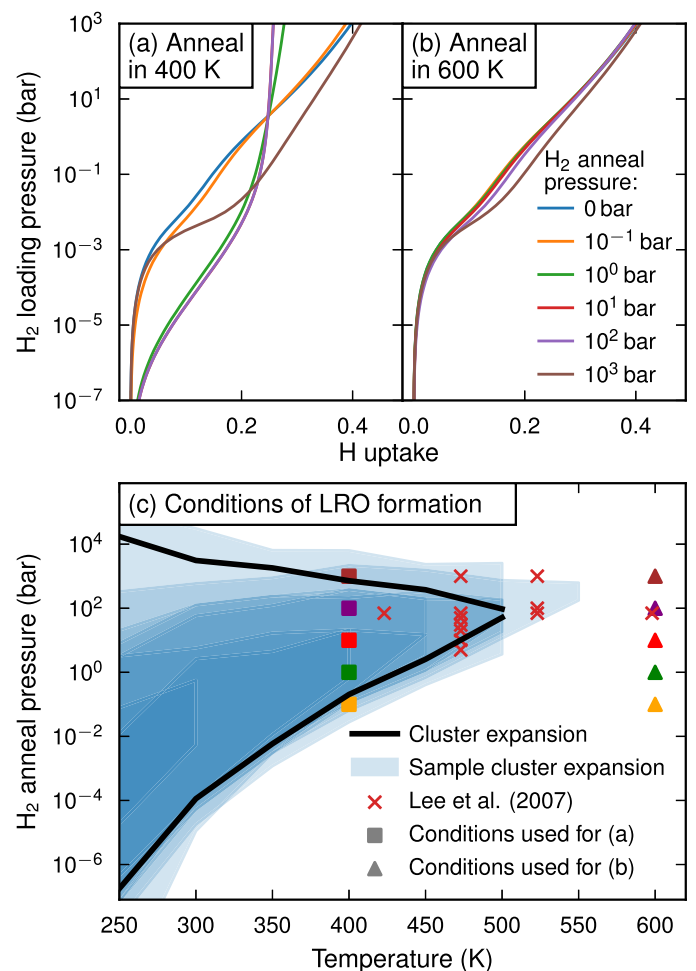


Fig. 8. Impact of annealing conditions on absorption of H in Pd–Au with 25% Au at 300 K. After annealing in 400 K (a), the isotherms exhibit a markedly different behavior if the H_2 pressure during annealing was between 1 and 100 bar (the red 10 bar isotherm is hidden under the green 1 bar isotherm). After annealing in 600 K (b), the isotherms are almost identical regardless of H_2 exposure during annealing. The origin of the change in isotherm in (a) is the formation of LRO under certain conditions as quantified in (c). The CE predicts that LRO will form in full equilibrium when Pd–Au with 25% Au is subjected to H_2 pressure and temperature corresponding to the area between the black lines. The corresponding area predicted with ten sampled CEs is indicated with transparent blue, one per CE. Darker color thus means more cluster expansion predict order formation at that point. Out of these ten cluster expansion, two have a critical temperature too low to be visible in this figure. The conditions investigated by Lee *et al.* [29] with signs of order formation in Pd–Au with 19% Au are indicated with red crosses. Colored squares and triangles indicate the annealing conditions for isotherms in (a) and (b), respectively.

are required to impact the system at 600 K compared to 400 K, because at constant pressure when the temperature goes up, the hydrogen content in the material goes down. Nevertheless, when the annealing pressure is 100 bar, the hydrogen content in the system is about 14% during annealing, but the 300 K isotherm is still virtually unaffected. Only when the annealing pressure reaches 1,000 bar (leading to approximately 26% hydrogen in the system during annealing), is the isotherm clearly distinguishable from the isotherm of Pd–Au annealed in vacuum, and even then the difference is small.

This picture emerges more comprehensively if we study the hydrogen absorbed at 300 K and specific partial pressures (Fig. S11): the content of hydrogen is virtually independent of annealing conditions as long as the phase transition to the L_{12} phase does not occur. Very high annealing pressures, on the order of 10–1000 bar,

are required to achieve a significant impact on the content of absorbed hydrogen unless the ordered L_{12} phase is formed.

It is worth stressing that while hydrogen uptake at moderate pressure is enhanced by LRO formation, we observe a different trend in Sect. 3.4; SRO formation decreases the hydrogen uptake unless the pressure is very low. It is thus advisable not to speak in too general terms about the impact of chemical order on hydrogen solubility, because it depends on the details of the chemical order as well as the H_2 pressure at which the solubility is assessed.

Given that the chemical ordering of the L_{12} phase thus has a significant impact on the nature of absorption of H_2 in Pd–Au, it may have a notable impact on any utilization thereof. We therefore estimate the conditions during which this long-range ordered phase will form (Fig. 8c). Our CE indicates that the ordered structure starts to form below approximately 500 K with a H_2 pressure between approximately 50 and 100 bar. The H_2 pressure range where LRO forms then widens quickly as temperature is decreased, but slower kinetics will of course inhibit order formation at too low temperatures. Lee *et al.* [29], who studied Pd–Au with 19% Au, assumed that distinct isotherms are a fingerprint of LRO, and while the purpose of their study was not to map out the conditions under which order emerges, their observations are qualitatively consistent with our CE (red crosses in Fig. 8c), but with a higher critical temperature (with LRO persisting up to at least 598 K). It thus seems likely that our CE underestimates the critical temperature by at least 100 K. By repeating the same calculations with 10 different cluster expansion (blue areas in Fig. 8c), we observe qualitatively the same behavior but find that both the critical temperature and the pressure range are very sensitive to small variations in the ECIs. Although none of the sampled cluster expansion exhibit a critical temperature above 600 K, it should be clear that small errors not captured by the CE approach (such as neglect of vibrations or the choice of exchange-correlation functional used to calculate the training data) may cause an error of this magnitude.

4. Conclusions

We have comprehensively investigated the impact of chemical order on hydrogenation of Pd–Au alloys using a computational approach based on DFT calculations, CE models, and MC simulations. Although relatively large relaxations from octahedral hydrogen sites hamper the ability of the CE models to exactly reproduce formation energies calculated with DFT, we found that our CE reproduced thermodynamic properties of Pd–Au–H that are well-established experimentally, with a quantitative agreement on par with what can be expected from a CE approach. This applies especially given the large impact of small changes in the ECIs, which is likely always inherent in this approach or indeed any other approach for deriving phase diagrams from interatomic potentials or first-principles data. Vibrational contributions, including the zero-point energy, can sometimes play an important role in hydrides due to the low mass of hydrogen, but inclusion of these effects would have been computationally prohibitive. Moreover, we note that tetrahedral hydrogen sites can play a role, although they are usually energetically much less favorable than octahedral sites [24,42]. These effects may contribute to some of the quantitative disagreement with experiment since especially vibrations have been shown to have a notable impact on phase diagrams [55–57].

Our results provide a rationale for the experimental observation that absorption/desorption isotherms are relatively stable over time; as long as the L_{12} phase does not form, isotherms will stay similar even if chemical order changes. This is manifested by the similarity between isotherms in random and para-equilibrium. Our results predict that a small reduction in the ability to absorb hydrogen may be observed if Pd–Au annealed at a very high temper-

ature is allowed to reach equilibrium at a much lower temperature. We emphasize that the present results are strictly valid only for the bulk material, and do not take into account potentially important effects such as agglomeration of hydrogen in grain boundaries, surface fouling or surface segregation, which should be kept in mind when comparing with experiment.

Under long-term exposure to hydrogen, however, the situation changes substantially. The emergence of the ordered L_{12} phase introduces complexity in the phase diagram, and Pd–Au stored at room temperature and, say, 1 mbar H_2 may over time exhibit very different absorption isotherms, as the result of emerging LRO. The hydrogen content in air is of course orders of magnitude lower than what we predict is required for this phase to form, but repeated exposure to high H_2 pressures may result in formation of LRO and an altered isotherm. Such conditions are found for example in membrane reactors for hydrogen gas production [58]. While we did not address kinetic aspects in this study, earlier experiments provide an approximate time scale for the transformation, as samples annealed at 523 K were observed to exhibit a gradual transition over many hours [29].

Does the LRO vanish when the hydrogen is removed? This question is difficult to answer, because our simulation approach is not able to describe the kinetic stability of the ordered phase in absence of hydrogen (or vice versa). We do predict that the L_{12} phase is the ground state at this composition also in absence of hydrogen, but its critical temperature is well below 300 K. It may, however, be noted that there are (hydrogen-free) Pd–Au phase diagrams in the literature where this phase is expected to form above room temperature [47,48,51], that is, even without exposure to hydrogen. Although the existence of this phase, let alone its critical temperature, remains debated, it seems reasonable to assume that the L_{12} phase might be fairly stable at room temperature even after hydrogen is removed. One should note that time-dependent annealing experiments suggest that order→disorder and disorder→order transitions proceed on similar time scales [29]. In combination with the exponential temperature dependence of the diffusivity, one can thus expect the time-temperature history of, e.g., a membrane reactor, to play a crucial role.

The emergence of a different isotherm upon ordering might constitute a challenge as the sensor would have a different readout at the same H_2 pressure. It may, however, also present an opportunity. The ordered phase absorbs significantly more hydrogen at low pressures. A sensor consisting of the ordered phase is thus likely (depending on the nature of the readout) to be significantly more sensitive to small changes in H_2 pressure. If the phase is sufficiently stable, this may provide a relatively simple way to improve a Pd–Au hydrogen sensor—annealing in hydrogen to boost sensitivity.

Declaration of Competing Interest

The authors declare that they have no known competing financial interests or personal relationships that could have appeared to influence the work reported in this paper.

Acknowledgments

This work was funded by the Knut and Alice Wallenberg Foundation (grant numbers 2014.0226, 2015.0055), the Swedish Research Council (grant numbers 2018-06482, 2020-04935), and the Swedish Foundation for Strategic Research (grant number RMA15-0052). The computations were enabled by resources provided by the Swedish National Infrastructure for Computing (SNIC) at NSC, C3SE and PDC partially funded by the Swedish Research Council (grant number 2018-05973). We thank Dr. Jonatan Wårdh for helpful discussions.

Supplementary material

Supplementary material associated with this article can be found, in the online version, at [10.1016/j.actamat.2021.116893](https://doi.org/10.1016/j.actamat.2021.116893)

References

- [1] A. Schneemann, J.L. White, S. Kang, S. Jeong, L.F. Wan, E.S. Cho, T.W. Heo, D. Prendergast, J.J. Urban, B.C. Wood, M.D. Allendorf, V. Stavila, Nanostructured metal hydrides for hydrogen storage, *Chemical Reviews* 118 (22) (2018) 10775–10839, doi:[10.1021/acs.chemrev.8b00313](https://doi.org/10.1021/acs.chemrev.8b00313).
- [2] C. Wadell, S. Syrenova, C. Langhammer, Plasmonic hydrogen sensing with nanostructured metal hydrides, *ACS Nano* 8 (12) (2014) 11925–11940, doi:[10.1021/nn505804f](https://doi.org/10.1021/nn505804f).
- [3] I. Darmadi, F.A.A. Nugroho, C. Langhammer, High-Performance Nanostructured Palladium-Based Hydrogen Sensors—Current Limitations and Strategies for Their Mitigation, *ACS Sensors* 5 (11) (2020) 3306–3327, doi:[10.1021/acssensors.0c02019](https://doi.org/10.1021/acssensors.0c02019).
- [4] T.C. Narayan, F. Hayee, A. Baldi, A.L. Koh, R. Sinclair, J.A. Dionne, Direct visualization of hydrogen absorption dynamics in individual palladium nanoparticles, *Nature Communications* 8 (1) (2017) 1–8, doi:[10.1038/ncomms14020](https://doi.org/10.1038/ncomms14020).
- [5] F.A. Nugroho, I. Darmadi, L. Cusinato, A. Susarrey-Arce, H. Schreuders, L.J. Bannenberg, A.B. da Silva Fanta, S. Kadkhodazadeh, J.B. Wagner, T.J. Antosiewicz, et al., Metal–polymer hybrid nanomaterials for plasmonic ultrafast hydrogen detection, *Nature Materials* 18 (5) (2019) 489–495, doi:[10.1038/s41563-019-0325-4](https://doi.org/10.1038/s41563-019-0325-4).
- [6] I. Darmadi, A. Stolaš, I. Östergren, B. Berke, F.A.A. Nugroho, M. Minelli, S. Lerch, I. Tanyeli, A. Lund, O. Andersson, V.P. Zhdanov, M. Liebi, K. Moth-Poulsen, C. Müller, C. Langhammer, Bulk-processed Pd nanocube-poly(methyl methacrylate) nanocomposites as plasmonic plastics for hydrogen sensing, *ACS Applied Nano Materials* 3 (8) (2020) 8438–8445, doi:[10.1021/acsnano.0c01907](https://doi.org/10.1021/acsnano.0c01907).
- [7] T.B. Flanagan, W.A. Oates, The palladium–hydrogen system, *Annual Review of Materials Science* 21 (1) (1991) 269–304, doi:[10.1146/annurev.ms.21.080191.001413](https://doi.org/10.1146/annurev.ms.21.080191.001413).
- [8] R. Griessen, N. Strohfeldt, H. Giessen, Thermodynamics of the hybrid interaction of hydrogen with palladium nanoparticles, *Nature Materials* 15 (3) (2016) 311–317, doi:[10.1038/nmat4480](https://doi.org/10.1038/nmat4480).
- [9] S. Syrenova, C. Wadell, F.A. Nugroho, T.A. Gschneidner, Y.A.D. Fernandez, G. Nalin, D. Świtlik, F. Westerlund, T.J. Antosiewicz, V.P. Zhdanov, et al., Hydride formation thermodynamics and hysteresis in individual Pd nanocrystals with different size and shape, *Nature Materials* 14 (12) (2015) 1236–1244, doi:[10.1038/nmat4409](https://doi.org/10.1038/nmat4409).
- [10] A. Maeland, T.B. Flanagan, X-ray and thermodynamic studies of the absorption of hydrogen by gold–palladium alloys, *The Journal of Physical Chemistry* 69 (10) (1965) 3575–3581, doi:[10.1021/j100894a054](https://doi.org/10.1021/j100894a054).
- [11] S. Luo, D. Wang, T.B. Flanagan, Thermodynamics of hydrogen in fcc Pd–Au alloys, *The Journal of Physical Chemistry B* 114 (18) (2010) 6117–6125, doi:[10.1021/jp100858r](https://doi.org/10.1021/jp100858r).
- [12] C. Wadell, F.A.A. Nugroho, E. Lidström, B. Iandolo, J.B. Wagner, C. Langhammer, Hysteresis-Free Nanoplasmonic Pd–Au Alloy Hydrogen Sensors, *Nano Letters* 15 (5) (2015) 3563–3570, doi:[10.1021/acs.nanolett.5b01053](https://doi.org/10.1021/acs.nanolett.5b01053).
- [13] F.A.A. Nugroho, I. Darmadi, V.P. Zhdanov, C. Langhammer, Universal scaling and design rules of hydrogen-induced optical properties in Pd and Pd–alloy nanoparticles, *ACS Nano* 12 (10) (2018) 9903–9912, doi:[10.1021/acsnano.8b02835](https://doi.org/10.1021/acsnano.8b02835).
- [14] R.J. Westerwaal, J.S.A. Rooijmans, L. Leclercq, D.G. Gheorghe, T. Radeva, L. Mooij, T. Mak, L. Polak, M. Slaman, B. Dam, T. Rasing, Nanostructured Pd–Au based fiber optic sensors for probing hydrogen concentrations in gas mixtures, *International Journal of Hydrogen Energy* 38 (10) (2013) 4201–4212, doi:[10.1016/j.ijhydene.2012.12.146](https://doi.org/10.1016/j.ijhydene.2012.12.146).
- [15] L.J. Bannenberg, F.A.A. Nugroho, H. Schreuders, B. Norder, T.T. Trinh, N.-J. Steinke, A.A. van Well, C. Langhammer, B. Dam, Direct comparison of pdau alloy thin films and nanoparticles upon hydrogen exposure, *ACS Applied Materials & Interfaces* 11 (17) (2019) 15489–15497, doi:[10.1021/acsmi.8b22455](https://doi.org/10.1021/acsmi.8b22455).
- [16] Y. Pak, Y. Jeong, N. Alala, H. Kim, J. Chae, J.-W. Min, A.A.S. Devi, S. Mitra, D.H. Lee, Y. Kumaresan, W. Park, T.-W. Kim, I.S. Roqan, G.-Y. Jung, Highly stable and ultrafast hydrogen gas sensor based on 15 nm nanogaps switching in a palladium-gold nanoribbons array, *Advanced Materials Interfaces* 6 (4) (2019) 1801442, doi:[10.1002/admi.201801442](https://doi.org/10.1002/admi.201801442).
- [17] A.J. Berry, LV1—The occlusion of hydrogen by the palladium–gold alloys, *Journal of the Chemical Society, Transactions* 99 (1911) 463–466, doi:[10.1039/CT9119900463](https://doi.org/10.1039/CT9119900463).
- [18] J. Schniedermann, Lichtelektrischer und thermoelektrischer Effekt wasserstoffbeladener Palladium–Silber und Palladium–Goldlegierungen, *Annalen der Physik* 405 (7) (1932) 761–779, doi:[10.1002/andp.19324050702](https://doi.org/10.1002/andp.19324050702).
- [19] Y. Sakamoto, F.L. Chen, M. Ura, T.B. Flanagan, Thermodynamic properties for solution of hydrogen in palladium-based binary alloys, *Berichte der Bunsengesellschaft für physikalische Chemie* 99 (6) (1995) 807–820, doi:[10.1002/bbpc.19950990605](https://doi.org/10.1002/bbpc.19950990605).
- [20] Y. Fukai, *The metal–hydrogen system: basic bulk properties*, 21, Springer Science & Business Media, 2006.
- [21] A. Pundt, R. Kirchheim, Hydrogen in metals: Microstructural aspects, *Annual Review of Materials Research* 36 (1) (2006) 555–608, doi:[10.1146/annurev.matsci.36.090804.094451](https://doi.org/10.1146/annurev.matsci.36.090804.094451).
- [22] W. Huang, S.M. Opalka, D. Wang, T.B. Flanagan, Thermodynamic modelling of the Cu–Pd–H system, *Calphad* 31 (3) (2007) 315–329, doi:[10.1016/j.calphad.2007.02.002](https://doi.org/10.1016/j.calphad.2007.02.002).
- [23] J.-M. Joubert, S. Thiébaud, A thermodynamic description of the system Pd–Rh–H–D–T, *Acta Materialia* 59 (4) (2011) 1680–1691, doi:[10.1016/j.actamat.2010.11.035](https://doi.org/10.1016/j.actamat.2010.11.035).
- [24] M. Mamatkulov, V.P. Zhdanov, Suppression of hysteresis in absorption of hydrogen by a Pd–Au alloy, *Phys. Rev. E* 101 (2020) 042130, doi:[10.1103/PhysRevE.101.042130](https://doi.org/10.1103/PhysRevE.101.042130).
- [25] A. Hultgren, *Isothermal transformation of austenite*, *Transactions of the American Society for Metals* 39 (1947) 915–1005.
- [26] M. Hillert, J. Ågren, On the definitions of paraequilibrium and ortho-equilibrium, *Scripta Materialia* 50 (5) (2004) 697–699, doi:[10.1016/j.scriptamat.2003.11.020](https://doi.org/10.1016/j.scriptamat.2003.11.020).
- [27] T.B. Flanagan, W. Oates, Para-equilibrium Phase Diagrams, $\mu_H - X_M$, for Pd Alloy–H Systems, *Journal of Phase Equilibria and Diffusion* 40 (2) (2019) 285–290, doi:[10.1007/s11669-019-00724-0](https://doi.org/10.1007/s11669-019-00724-0).
- [28] D.E. Nanu, Y. Deng, A.J. Böttger, Unified approach for cluster variation method calculations of phase diagrams in fcc substitutional alloys with interstitial species, *Physical Review B* 74 (2006) 014113, doi:[10.1103/PhysRevB.74.014113](https://doi.org/10.1103/PhysRevB.74.014113).
- [29] S.-M. Lee, H. Noh, T.B. Flanagan, S. Luo, Hydrogen-induced lattice rearrangement of a Pd_{0.81}Au_{0.19} alloy, *Journal of Physics: Condensed Matter* 19 (32) (2007) 326222, doi:[10.1088/0953-8984/19/32/326222](https://doi.org/10.1088/0953-8984/19/32/326222).
- [30] N. Chandrasekhar, D.S. Sholl, Computational study of hydrogen induced lattice rearrangement and its influence on hydrogen permeance in Pd–Au alloys, *Journal of Alloys and Compounds* 609 (2014) 244–252, doi:[10.1016/j.jallcom.2014.04.156](https://doi.org/10.1016/j.jallcom.2014.04.156).
- [31] L. Semidey-Flecha, D.S. Sholl, Combining density functional theory and cluster expansion methods to predict H₂ permeance through Pd-based binary alloy membranes, *The Journal of Chemical Physics* 128 (14) (2008) 144701, doi:[10.1063/1.2900558](https://doi.org/10.1063/1.2900558).
- [32] N. Bourgeois, P. Cenedese, J.-C. Crivello, J.-M. Joubert, Pd–H and Ni–H phase diagrams using cluster variation method and Monte Carlo simulation, *Philosophical Magazine* 99 (19) (2019) 2376–2392, doi:[10.1080/14786435.2019.1628367](https://doi.org/10.1080/14786435.2019.1628367).
- [33] N.S.H. Gunda, A. Van der Ven, First-principles insights on phase stability of titanium interstitial alloys, *Physical Review Materials* 2 (2018) 083602, doi:[10.1103/PhysRevMaterials.2.083602](https://doi.org/10.1103/PhysRevMaterials.2.083602).
- [34] B. Ouyang, T. Chakraborty, N. Kim, N.H. Perry, T. Mueller, N.R. Aluru, E. Ertekin, Cluster Expansion Framework for the Sr(Ti_{1-x}Fe_x)O_{3-x/2} (0 < x < 1) Mixed Ionic Electronic Conductor: Properties Based on Realistic Configurations, *Chemistry of Materials* 31 (9) (2019) 3144–3153, doi:[10.1021/acs.chemmater.8b04285](https://doi.org/10.1021/acs.chemmater.8b04285).
- [35] G.L.W. Hart, R.W. Forcade, Algorithm for generating derivative structures, *Physical Review B* 77 (2008) 224115, doi:[10.1103/PhysRevB.77.224115](https://doi.org/10.1103/PhysRevB.77.224115).
- [36] M. Ångqvist, W.A. Muñoz, J.M. Rahm, E. Fransson, C. Durniak, P. Rozyczko, T.H. Rod, P. Erhart, Ictet – a python library for constructing and sampling alloy cluster expansions, *Advanced Theory and Simulations* 2 (7) (2019) 1900015, doi:[10.1002/adts.201900015](https://doi.org/10.1002/adts.201900015).
- [37] G. Kresse, J. Furthmüller, Efficiency of ab-initio total energy calculations for metals and semiconductors using a plane-wave basis set, *Computational Materials Science* 6 (1) (1996) 15–50, doi:[10.1016/0927-0256\(96\)00008-0](https://doi.org/10.1016/0927-0256(96)00008-0).
- [38] G. Kresse, D. Joubert, From ultrasoft pseudopotentials to the projector augmented-wave method, *Physical Review B* 59 (1999) 1758–1775, doi:[10.1103/PhysRevB.59.1758](https://doi.org/10.1103/PhysRevB.59.1758).
- [39] M. Dion, H. Rydberg, E. Schröder, D.C. Langreth, B.I. Lundqvist, Van der Waals density functional for general geometries, *Phys. Rev. Lett.* 92 (2004) 246401, doi:[10.1103/PhysRevLett.92.246401](https://doi.org/10.1103/PhysRevLett.92.246401).
- [40] K. Berland, P. Hyldgaard, Exchange functional that tests the robustness of the plasmon description of the van der Waals density functional, *Physical Review B* 89 (2014) 035412, doi:[10.1103/PhysRevB.89.035412](https://doi.org/10.1103/PhysRevB.89.035412).
- [41] J. Sanchez, F. Ducastelle, D. Gratias, Generalized cluster description of multi-component systems, *Physica A: Statistical Mechanics and its Applications* 128 (1) (1984) 334–350, doi:[10.1016/0378-4371\(84\)90096-7](https://doi.org/10.1016/0378-4371(84)90096-7).
- [42] D. Nanu, W. Legerstee, S. Ejit, W. Haije, J. Vente, M. Tucker, A. Böttger, Insights into the relation between crystal structure and deuterium desorption characteristics of Pd–Au–D alloys, *Acta Materialia* 56 (20) (2008) 6132–6140, doi:[10.1016/j.actamat.2008.08.045](https://doi.org/10.1016/j.actamat.2008.08.045).
- [43] T. Mueller, G. Ceder, Bayesian approach to cluster expansions, *Physical Review B* 80 (2009) 024103, doi:[10.1103/PhysRevB.80.024103](https://doi.org/10.1103/PhysRevB.80.024103).
- [44] D. Foreman-Mackey, D.W. Hogg, D. Lang, J. Goodman, emcee: The MCMC hammer, *Publications of the Astronomical Society of the Pacific* 125 (925) (2013) 306–312, doi:[10.1086/670067](https://doi.org/10.1086/670067).
- [45] B. Sadigh, P. Erhart, Calculation of excess free energies of precipitates via direct thermodynamic integration across phase boundaries, *Physical Review B* 86 (2012) 134204, doi:[10.1103/PhysRevB.86.134204](https://doi.org/10.1103/PhysRevB.86.134204).
- [46] B. Sadigh, P. Erhart, A. Stukowski, A. Caro, E. Martinez, L. Zepeda-Ruiz, Scalable parallel monte carlo algorithm for atomistic simulations of precipitation in alloys, *Physical Review B* 85 (2012) 184203, doi:[10.1103/PhysRevB.85.184203](https://doi.org/10.1103/PhysRevB.85.184203).
- [47] Y. Matsuo, A. Nagasawa, J. Kakinoki, Ordered Alloys of the Gold–Palladium System. II. Electron Diffraction Study on Evaporated AuPd₃ Films, *Journal of the Physical Society of Japan* 21 (12) (1966) 2633–2637, doi:[10.1143/JPSJ.21.2633](https://doi.org/10.1143/JPSJ.21.2633).
- [48] Y. Kawasaki, S. Ino, S. Ogawa, Electron diffraction study on the superlattice formation in the gold–palladium alloy system, *Journal of the Physical Society of Japan* 30 (6) (1971) 1758–1759, doi:[10.1143/JPSJ.30.1758](https://doi.org/10.1143/JPSJ.30.1758).

- [49] J. Nelayah, N.T. Nguyen, D. Alloyeau, G.Y. Wang, C. Ricolleau, Long-range chemical orders in Au–Pd nanoparticles revealed by aberration-corrected electron microscopy, *Nanoscale* 6 (2014) 10423–10430, doi:[10.1039/C4NR01427H](https://doi.org/10.1039/C4NR01427H).
- [50] S.V. Barabash, V. Blum, S. Müller, A. Zunger, Prediction of unusual stable ordered structures of Au–Pd alloys via a first-principles cluster expansion, *Physical Review B* 74 (2006) 035108, doi:[10.1103/PhysRevB.74.035108](https://doi.org/10.1103/PhysRevB.74.035108).
- [51] F. Berthier, B. Legrand, Analysis of Au–Pd driving forces via the effective site energy model: LRO, antisites and enthalpy of permutation, *Journal of Physics: Condensed Matter* 32 (35) (2020) 354001, doi:[10.1088/1361-648x/ab87ce](https://doi.org/10.1088/1361-648x/ab87ce).
- [52] E. Wicke, J. Blaurock, New experiments on and interpretations of hysteresis effects of Pd–D₂ and Pd–H₂, *Journal of the Less Common Metals* 130 (1987) 351–363, doi:[10.1016/0022-5088\(87\)90129-9](https://doi.org/10.1016/0022-5088(87)90129-9).
- [53] F.E. Wagner, M. Karger, F. Pröbst, B. Schüttler, Interaction of Hydrogen with Substitutional Solute Metals in the β -Phase of the Palladium–Hydrogen System, Springer US, Boston, MA, pp. 581–588. [10.1007/978-1-4684-7630-9_82](https://doi.org/10.1007/978-1-4684-7630-9_82)
- [54] C.G. Sonwane, J. Wilcox, Y.H. Ma, Solubility of hydrogen in PdAg and PdAu binary alloys using density functional theory, *The Journal of Physical Chemistry B* 110 (48) (2006) 24549–24558, doi:[10.1021/jp064507t](https://doi.org/10.1021/jp064507t).
- [55] A. van de Walle, G. Ceder, The effect of lattice vibrations on substitutional alloy thermodynamics, *Reviews of Modern Physics* 74 (2002) 11–45, doi:[10.1103/RevModPhys.74.11](https://doi.org/10.1103/RevModPhys.74.11).
- [56] A. Böttger, D. Nanu, A. Marashdeh, The γ -Fe[N] and γ' -Fe₄N_{1-x} phase boundaries in high-nitrogen steels: The cube cluster approximation and the effect of vibrational energy contributions, *Computational Materials Science* 95 (2014) 8–12, doi:[10.1016/j.commatsci.2014.07.004](https://doi.org/10.1016/j.commatsci.2014.07.004).
- [57] M. Gren, E. Fransson, M. Ångqvist, P. Erhart, G. Wahnström, Modeling of vibrational and configurational degrees of freedom in hexagonal and cubic tungsten carbide at high temperatures, *Physical Review Materials* 5 (3) (2021) 033804, doi:[10.1103/PhysRevMaterials.5.033804](https://doi.org/10.1103/PhysRevMaterials.5.033804).
- [58] G. Bernardo, T. Araújo, T. da Silva Lopes, J. Sousa, A. Mendes, Recent advances in membrane technologies for Hydrogen purification, *International Journal of Hydrogen Energy* 45 (12) (2020) 7313–7338 Hydrogen separation/purification via membrane technology., doi:[10.1016/j.ijhydene.2019.06.162](https://doi.org/10.1016/j.ijhydene.2019.06.162). Hydrogen separation/purification via membrane technology

A tale of two phase diagrams: Interplay of ordering and hydrogen uptake in Pd–Au–H

J. Magnus Rahm, Joakim Löfgren, Erik Fransson, and Paul Erhart

Contents

Notes	2
SN1. Structure generation and DFT calculations	2
SN2. Alloy cluster expansion construction	2
SN3. Monte Carlo simulations	3
SN4. Conversion between chemical potential and partial pressure of hydrogen	4
SN5. Short and long range order quantification	4
SN6. Phase diagram construction	5
Figures	6
S1. Plateau pressures in pure Pd	6
S2. Relaxations and shearing in PdAu:H	6
S3. RMSE, AIC, and BIC as a function of cutoffs in the cluster expansion	7
S4. Prior and posterior distributions for hyper parameters	8
S5. Corner plot for the most short-ranged ECIs	9
S6. Critical temperatures of L1 ₂ with and without hydrogen	10
S7. Change in uptake of hydrogen and SRO with annealing temperature	10
S8. SRO in full equilibrium	11
S9. LRO in full equilibrium	11
S10. Phase diagram in full equilibrium at 250 K and 500 K	12
S11. Change in hydrogen uptake with annealing temperature and H ₂ pressure	12
References	13

Notes

Supplementary Note 1: Structure generation and DFT calculations

Structures were generated by exhaustive enumeration (1, 2) of supercells of the primitive structure with up to 12 atoms in the cell (6 per sublattice). The limited supercell size precludes structures with Au concentration between 0 and 16.67% but as this is a composition interval of particular interest, we generated an additional 200 structures in this interval having up to 32 atoms in the cell, heuristically chosen so as to properly span the space of cluster vectors. Finally, in order to properly describe the important limit of pure Pd hydride, we generated 367 structures without Au, having up to 24 atoms in the cell.

For generation of training data, we used the projector augmented wave formalism as implemented in the Vienna ab initio simulation package (version 5.4.1, PAW 2015) (3, 4) with the vdW-DF-cx exchange-correlation functional (5, 6). Wave functions were expanded in a plane wave basis set with a cutoff of 400 eV, the Brillouin zone (BZ) was sampled with a Γ -centered grid with a \mathbf{k} point spacing of 0.2 \AA^{-1} , and occupations were set using Gaussian smearing with a width of 0.1 eV. Atomic positions and cell shape were relaxed until residual forces were below 25 meV/\AA and stresses below 1 kbar. Once converged, we ran an additional single-point calculation with a \mathbf{k} point spacing of 0.1 \AA^{-1} and the BZ was integrated using the tetrahedron method with Blöchl corrections.

Supplementary Note 2: Alloy cluster expansion construction

In an alloy cluster expansion (CE), the energy of a configuration of atoms σ is decomposed into contributions from single sites (“singlets”), pairs of sites, triplets of sites, etc, commonly referred to as clusters. Denoting such clusters α , the energy can be expressed as

$$E(\sigma) = J_0 + \sum_{\alpha} J_{\alpha} m_{\alpha} \langle \Pi_{\alpha}(\sigma) \rangle_{\alpha}, \quad (1)$$

where the effective cluster interaction (ECI) J_{α} measures the energy associated with the cluster α (with J_0 being a constant, the “zerolet”), m_{α} is the number of symmetrically equivalent clusters α , and $\langle \Pi_{\alpha}(\sigma) \rangle_{\alpha}$ quantifies the chemical ordering of the clusters α . Specifically, $\langle \Pi_{\alpha}(\sigma) \rangle_{\alpha}$ is an average over all symmetrically equivalent clusters α , where each term is a product of so-called point functions,

$$\Pi_{\alpha}(\sigma) = \prod_{i \in \alpha} \Theta_i, \quad (2)$$

meaning that the product runs over all lattice sites i in the cluster α . Here, we explicitly treat unoccupied interstitial sites as vacancies, which makes it possible to view the interstitial sublattice as an alloy. In our case, the point functions then take the value $\Theta_i = -1$ if site i is occupied by Au or H, or $\Theta_i = 1$ if site i is occupied by Pd or a vacancy (but the sublattices are distinct, meaning that, e.g., hydrogen cannot occupy a site on the Pd–Au sublattice).

Although it can be shown that this basis set forms a complete orthonormal basis and thus can be used to exactly express any function of the configuration σ (7), in practice it has to be truncated. Physical intuition tells us that clusters with few sites and short interatomic distances should be more important, and by analyzing the Akaike information criterion (AIC) and Bayesian Information Criterion (BIC) (8) (Figure S3), we found that it was sufficient to include pairs no more than $1.75a_0$ apart (where a_0 is the lattice parameter of the conventional (cubic) cell) and triplets that had all interatomic distances shorter than $1.25a_0$. With these cutoffs, we end up with 18 and 42 symmetrically distinct pairs and triplets, respectively.

The ECIs J_{α} were deduced by fitting the linear equation (1) to the energies calculated with density-functional theory (DFT) using a Bayesian approach (9). We assumed that the errors were normally distributed with variance σ_1^2 , and used an inverse gamma function as prior for σ_1 . Furthermore, we used Gaussian priors for the ECIs (having mean $\mu = 0$ and variance σ_2^2), and used an inverse gamma function as prior for σ_2 . (We note that the fitting process was largely insensitive to the choice of priors due to the large training data set.) We then sampled the posterior distribution using Markov chain Monte Carlo (MCMC) simulations as implemented in the EMCEE software (10) with 300 walkers and 417,000 MC steps (100 times the auto-correlation length). From the resulting posterior distributions, we constructed our final model as the average over the posterior distribution for each ECI (we used the average rather than the peak of the posterior since the posteriors were almost perfectly symmetric and the two measures therefore coincided to within less than 0.5 meV/formula unit (f.u.), and the average is insensitive to noise and choice of bins). All of the results presented below were obtained with this CE unless otherwise stated. In addition to this CE, we randomly selected 10 independent CEs from

the MCMC trajectory, which were used to investigate the impact of variations in the ECIs on thermodynamic properties of the model. For details on priors and posterior distributions, see [Figure S4–S5](#).

It is usually practical to fit CEs to mixing energies, defined such that the pure phases have zero mixing energy. In our system, we have four pure phases: Au and Pd with and without hydrogen. Only linear transformations are permissible from a thermodynamic perspective since only first-order terms cancel. This implies that only three (out of four) boundary points can be set strictly to zero. Here, we make the (intuitively logical) choice to set Pd, PdH and Au to zero, leaving AuH using the following definition of the mixing energy:

$$E_{\text{mix, DFT}}(\sigma) = E_{\text{DFT}}(\sigma)/N - [c_{\text{Pd}} - c_{\text{H}}] E_{\text{DFT}}(\text{Pd}) - c_{\text{H}} E_{\text{DFT}}(\text{PdH}) - c_{\text{Au}} E_{\text{DFT}}(\text{Au}) \quad (3)$$

where N is the number of f.u.s in the structure (i.e., the total number of Au and Pd atoms).

Generation of structures with exhaustive enumeration always yields disproportionately many structures close to 50% concentrations, as it corresponds to the largest number of symmetrically distinct structures. To counter this bias, we constrained the CE to always reproduce the mixing energy of Pd, PdH, and Au to their exact mixing energy values (0 meV/f.u. per definition).

A CE operates under the assumption that the atoms reside on a fixed lattice. In practice the effect of relaxation from the ideal lattice sites is, however, incorporated effectively through the fitting of the ECIs J_{α} . For this treatment of relaxation to be feasible, the relaxed structure must not deviate too strongly from the ideal lattice (11). An analysis of our DFT calculations revealed that in many structures, in particular those with a high Au content, relaxations from the ideal lattice sites were large, sometimes more than half the distance to the nearest neighbor on the other sublattice ([Figure S2a](#)). To avoid training the CE on data that is not well represented by a lattice model, we excluded all structure in which at least one atom had relaxed more than 0.5 Å from its ideal site, which is equivalent to approximately 25% of the distance to its nearest neighbor. Furthermore, the relaxed cell shape sometimes deviated from the cubic cell. In particular, pure AuH with 100% H is mechanically unstable and relaxes into a monoclinic structure (it should be noted that pure Au hydrides are considered unstable even under very high H₂ pressures (12, 13)). To further investigate the crystal structure, we therefore also analyzed the shearing of the cell. Here, we define the shear strain tensor ΔA by subtracting the volumetric strain from the Biot strain tensor (14) (defined as $\mathbf{U} - \mathbf{I}$, where \mathbf{U} is in turn defined by the polar decomposition of the deformation tensor, $\mathbf{F} = \mathbf{U}\mathbf{P}$), and a scalar measure of the strain is obtained by taking the Frobenius norm of ΔA . On average, higher concentrations of Au and H tend to increase the shear strain ([Figure S2b](#)).

Since structures with a very high Au content are not experimentally relevant except under fairly exotic conditions, we chose to exclude all structures with Au concentration above 50%. With the limitation to structures with no displacements larger than 0.5 Å and no Au content above 50%, all structures with a shear strain $\|\Delta A\|_{\text{F}} > 0.4$ were effectively excluded. In the end, we were left with 1,305 structures, out of which 1,255 were used for training the CE, with the remaining 50 used as test set to evaluate the performance of the final model.

The mixing energies (defined in [Equation 3](#)) span an energy range of approximately -100 meV/f.u. to 500 meV/f.u. (Fig. 1a in the main paper). This wide range of energies is a challenge for the CE model, since some of the important phenomena occur on a much more narrow energy scale. Consider, for example, the two-phase region of pure Pd hydride. This two-phase region is the result of a concave mixing energy curve between $c_{\text{H}} = 0$ and 0.67 (Fig. 1b in the main paper), and the distance between the lowest energy structures and the convex hull is at most a few meV/f.u. (with the limited cell size in our training data). Meanwhile, if we increase the Au content, relevant variations occur on a scale that is at least one order of magnitude larger. To ensure that the important variations at low Au content are properly captured, we multiplied the cluster vectors and target energies with a weight $w(c_{\text{Au}}) = 1 + 10(0.5 - c_{\text{Au}})$ prior to fitting, chosen to make the variations in mixing energy occur within the same order of magnitude over the full range of Au concentrations. We note that non-uniform weighting of structures as well as the imposing of constraints to exactly reproduce some structures is done at the cost of a larger error for other structures, and inevitably a larger root mean square error over the full test set. Yet, it is more important to capture the relevant aspects of the energy landscape properly rather than having the lowest possible root mean square error.

Supplementary Note 3: Monte Carlo simulations

Monte Carlo (MC) simulations were carried out according to a standard Metropolis scheme, in which the chemical identity of one or more atoms is changed in each step, and the change is accepted with probability $P = \min\{1, \exp(-\Delta\psi/k_{\text{B}}T)\}$. The change in the potential $\Delta\psi$ can be modified to account for different physical situations. Here, we used three different approaches.

The first approach is to sample the canonical ensemble by letting ψ be the change in potential energy, $\psi = E$, and always swap the identities of two unlike atoms on the same sublattice. This has the advantage of preserving

the overall concentration of the chemical species and is thus reminiscent of typical experimental conditions for the Pd–Au lattice. In the case of hydrogen, however, one experimentally controls the chemical potential rather than the concentration, and it becomes impossible to relate the conditions to a partial pressure of H₂ since the chemical potential is not an observable of the canonical ensemble.

Second, if we let $\psi = E + \mu_{\text{H}}N_{\text{H}}$, where μ_{H} and N_{H} are the chemical potential of hydrogen and the number of hydrogen atoms, respectively, we sample the grand canonical ensemble with respect to the H sublattice. In this case, the chemical potential of hydrogen is specified rather than the concentration, similar to experiment, and it is possible to relate the conditions to a partial pressure of H₂ (see [section 4](#)). Moreover, one has access to a free energy derivative since

$$\partial F / \partial c_{\text{H}} = \mu_{\text{H}}. \quad (4)$$

If we view vacancies as a chemical species, we may also refer to this as sampling in the semi-grand canonical (SGC) ensemble (with the difference in chemical potential simply being the chemical potential of hydrogen as the chemical potential of vacancies is zero) and this term will be used below.

Finally, we also used the variance-constrained semi-grand canonical (VCSGC) ensemble ([15](#), [16](#)), in which $\psi = E + Nk_{\text{B}}T\bar{\kappa}(c + \bar{\phi}/2)^2$, where $\bar{\kappa}$ and $\bar{\phi}$ control the variance and mean of the concentration c , respectively. With this approach we may, unlike the SGC, stabilize the system inside multi-phase regions and thereby integrate free energies across phase boundaries using the free energy derivative

$$\partial F / \partial c = -2Nk_{\text{B}}T\bar{\kappa}(\langle c \rangle + \bar{\phi}/2), \quad (5)$$

where $\langle c \rangle$ is the average observed concentration. By equating [Eq. \(4\)](#) and [\(5\)](#), we may also relate an observed state to an external partial pressure of H₂.

It should be noted that the two sublattices may be sampled in different ensembles in the same MC simulation. In this work, we have used several combinations of the three above-mentioned ensembles as will be detailed below. For each set of independent parameters, we ran 1,000 MC sweeps (1 sweep = N steps, where N is the number of sites in the cell), of which the first 50 were discarded to allow for equilibration. The simulations were commenced from a random H–vacancy sublattice with equimolar concentrations, whereas the starting configuration of the Pd–Au sublattice was either random, or, in the case of random equilibrium and para-equilibrium as well as for the simulation of isotherms, fixed in a predetermined configuration. The simulations were done with a supercell corresponding to $6 \times 6 \times 6$ times the conventional cell, for a total of 1,728 sites (864 per sublattice). All MC simulations were carried out with the MCHAMMER module of the ICET package ([1](#)).

Supplementary Note 4: Conversion between chemical potential and partial pressure of hydrogen

Experimentally, the chemical potential of hydrogen, $\mu_{\text{H}} = \frac{1}{2}\mu_{\text{H}_2}$, is controlled via the partial pressure of H₂, p_{H_2} . Treating H₂ as an ideal gas, we can write the following relation between its chemical potential and pressure,

$$\mu_{\text{H}_2}(T, p_{\text{H}_2}) = \mu_{\text{H}_2}^{\circ}(T) + k_{\text{B}}T \ln \frac{p_{\text{H}_2}}{p_{\text{H}_2}^{\circ}}. \quad (6)$$

Here, $p_{\text{H}_2}^{\circ}$ is a reference pressure and $\mu_{\text{H}_2}^{\circ}(T)$ is the temperature dependent chemical potential of H₂ at this reference pressure. The latter can in principle be evaluated with a combination of DFT calculations and thermochemical tables, but since small errors in $\mu_{\text{H}_2}^{\circ}(T)$ have a large impact on p_{H_2} , we chose to make a two-parameter fit. Specifically, we extracted experimental data of the partial pressures of the $\alpha \rightarrow \beta$ transition in pure Pd at different temperatures, and fitted a linear function to these $(\ln(p), T)$ data points. We then fitted a linear function to the points $(2\mu_{\text{H}}, T)$ at which we observed the phase transition in our own simulations. The conversion is then given by

$$p_{\text{H}_2} = \exp\left(\frac{2\mu_{\text{H}} + \Delta P(T)}{k_{\text{B}}T}\right) \quad (7)$$

where $\Delta P(T)$ is the difference between the two linear fits, specifically $\Delta P(T) = 1.2 \text{ meV/K} \cdot T - 0.3547 \text{ eV}$ (for more details, see [Figure S1](#)). It should be noted that breakdown of the ideal gas approximation at very high H₂ pressures will make our conversion between chemical potential and pressure increasingly inaccurate.

Supplementary Note 5: Short and long range order quantification

We quantify short-range order (SRO) with the Warren–Cowley order parameter,

$$\alpha_{\text{A-B}} = 1 - \frac{n_{\text{A-B}}}{Zc_{\text{A}}c_{\text{B}}}, \quad (8)$$

where A and B refer to the two species involved (Au and Pd or H and vacancy, depending on sublattice), n_{A-B} is the total number of unlike bonds $A-B$ in a certain shell (such as nearest neighbors), Z is the total number of bonds (regardless of decoration), and c_A and c_B is the overall concentration of A and B, respectively. To quantify SRO between the two sublattices, we generalize the above expression,

$$\alpha_{\text{Au/Pd-H/vac}} = 1 - \frac{n_{\text{Pd-H,Au-vac}}}{Z(c_{\text{H}}c_{\text{Pd}} + c_{\text{Au}}c_{\text{vac}})}, \quad (9)$$

where $n_{\text{Pd-H,Au-vac}}$ is the total number of pairs that are either Pd-H or Au-vacancy.

To quantify long-range order (LRO) on the Pd-Au sublattice, we use a standard expression for the structure factor,

$$S(\mathbf{q}) = \frac{1}{N^2} \sum_{ij} f_i f_j e^{-i\mathbf{q} \cdot (\mathbf{R}_i - \mathbf{R}_j)}, \quad (10)$$

where the sum runs over all pairs i, j of sites in the sublattice (with a total of N sites), \mathbf{R}_i is the position of atom i , and $f_i = 1$ if atom i is Au and -1 if it is Pd.

Supplementary Note 6: Phase diagram construction

Once mixing free energy curves $F_{\text{mix}}(c_{\text{H}}, c_{\text{Au}}, T)$ have been calculated from MC simulations, phase diagrams can be constructed by identifying the regions where the free energy curve lies above its convex hull. (This construction relies on the assumption that the interface between the two phases is incoherent; hysteresis stemming from coherency will in general increase the apparent solubility (17, 18).) The boundaries of these regions constitute the phase boundary, and to obtain a continuous phase boundary, we fitted, primarily as a guide to the eye, the observed boundary points to the function

$$f(c) = a \frac{2c - 1}{\ln c - \ln(1 - c)} + L(c) \quad (11)$$

where a is a fitting parameter and $L(c)$ is a fourth-order Redlich-Kister polynomial with five fitting parameters.

To construct the phase diagram in full equilibrium, we made MC simulations in which we sampled the VCSGC ensemble on both lattices. We thus had two independent parameters $\bar{\phi}$, one per sublattice, with which we could sweep (in steps of $\Delta\bar{\phi} = 0.04$) the full 2D concentration range. This yielded two partial free energy derivatives,

$$\frac{\partial F}{\partial c_{\text{Au}}} \quad \text{and} \quad \frac{\partial F}{\partial c_{\text{H}}}. \quad (12)$$

To compute the free energy, we may integrate Equation 12 along some 2D path. Ideally, the choice of integration path is unimportant; they should all yield the same result. Nevertheless, noise in the MC results can quickly accumulate, resulting in different results depending on integration path. Furthermore, a long integration path runs a higher risk of accumulating a lot of noise. To overcome these challenges, we defined a 2D grid of points between 0 and 70% H, and 0 and 50% Au, both in steps of 5%. We then linearly interpolated the free energy derivatives (Equation 12) on a denser grid (spacing 1%). Starting from a point on the sparse grid, we then defined 10 different integration paths to each point on the dense grid. These paths were constructed by taking the required number of steps needed in the c_{Au} and the c_{H} direction in a random order (following a ‘‘taxicab geometry’’). We averaged the results over these 10 paths, and constructed the convex hull and recorded all points on the dense grid that were on the convex hull. This process was repeated for all starting points on the sparse grid. In the end, each point on the dense grid had been recorded as belonging to the convex hull a certain number of times, between 0 and the number of starting points on the sparse grid. To finally plot the phase diagram, we removed all the points that had been recorded on the convex hull less than 5% of the point that had been recorded the most number of times, and finally plotted the result as a heat map with colors logarithmically dependent on how many times each point was recorded on the convex hull.

Finally isobars were drawn by identifying the points at which the interpolated derivatives $\partial F / \partial c_{\text{H}} = \mu_{\text{H}}$ attained the value corresponding to the sought pressure. Whenever these points crossed a multi-phase region, they were replaced with a straight line starting/ending where the isobar left/entered a single-phase region.

Figures

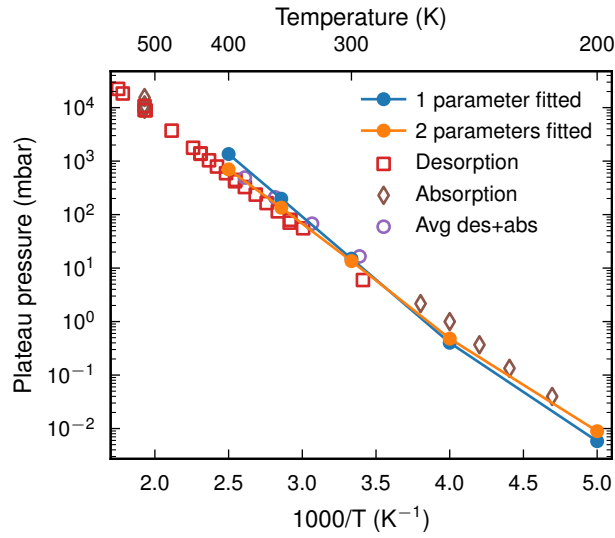


Figure S1: Plateau pressure in absorption and desorption isotherms of hydrogen in pure Pd. Red squares, brown diamonds and purple circles are, respectively, experimental desorption, absorption and average desorption/absorption pressures from the literature (19–23). Orange line is our two-parameter fit as described in the main paper. Blue line is a one-parameter fit, where the first-degree polynomial described in the main paper is replaced by a constant.

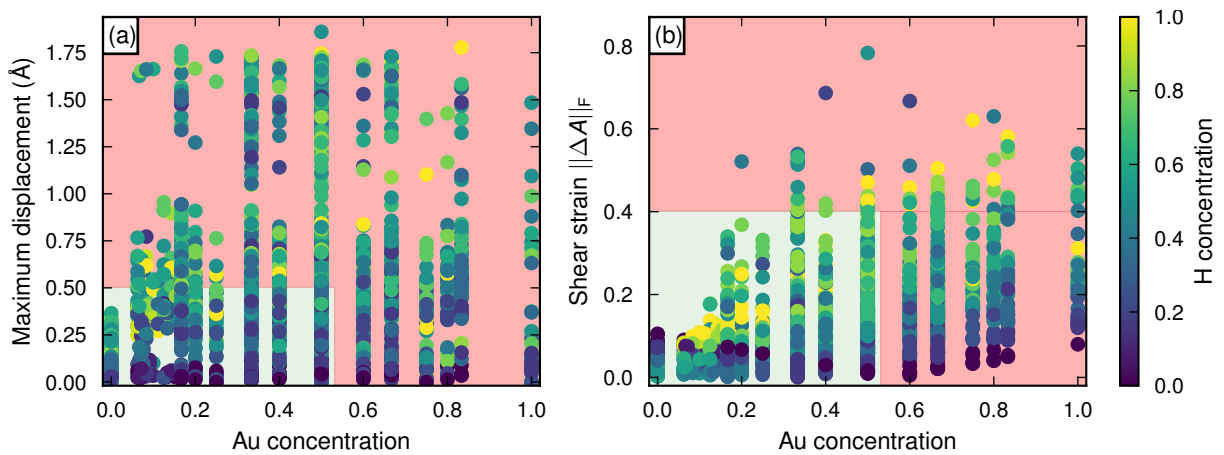


Figure S2: Relaxations from ideal rocksalt structure in PdAu:H. Relaxation is split in (a) maximum displacement from ideal lattice site among the atoms in the structure and (b) shearing of the cell as measured by the Frobenius norm of the shear part of the transformation $\|\Delta A\|_F$. Each dot represents one atomic structure, and its color represents the H content. Atomic structures in the light red areas were not used for training of the CE.

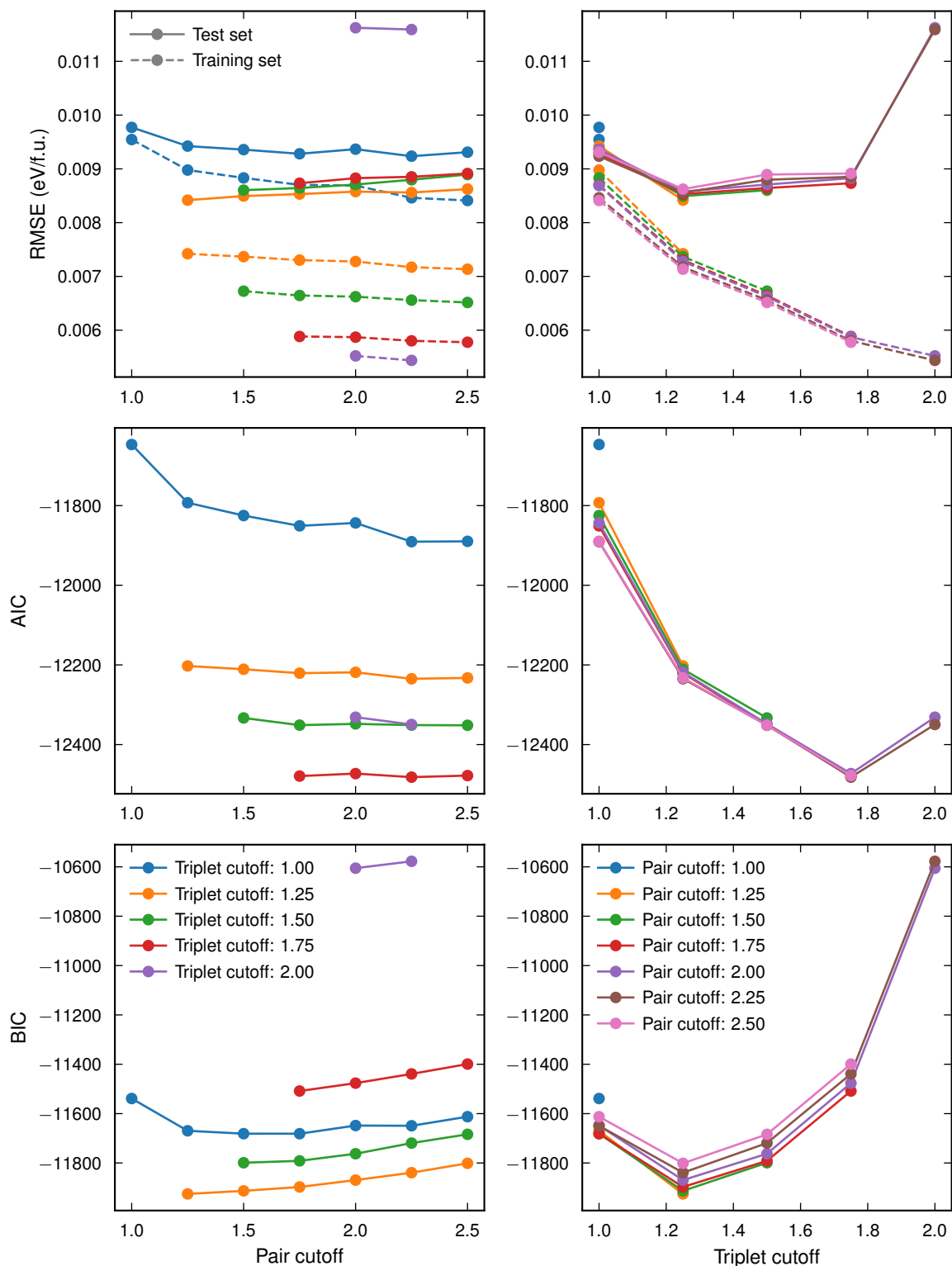


Figure S3: Root mean square error (RMSE, top row), Akaike information criterion (AIC, middle row), and Bayesian information criterion (BIC, bottom row) as a function of pair (left column) and triplet cutoff (right column) in the truncation of the CE. Cutoffs are given in units of the lattice parameter, and specify the longest allowed interatomic distance in the cluster. The different criteria paint slightly different pictures, but a pair cutoff at 1.75 was deemed reasonable as it provides a low RMSE in the test set and one of the lowest AIC and BIC values, and a triplet cutoff at 1.25 was chosen as it minimizes the RMSE of the training set and the BIC. To produce this data, the non-weighted training set was fitted with ordinary least squares, and the RMSE values are therefore slightly lower than for the final CE.

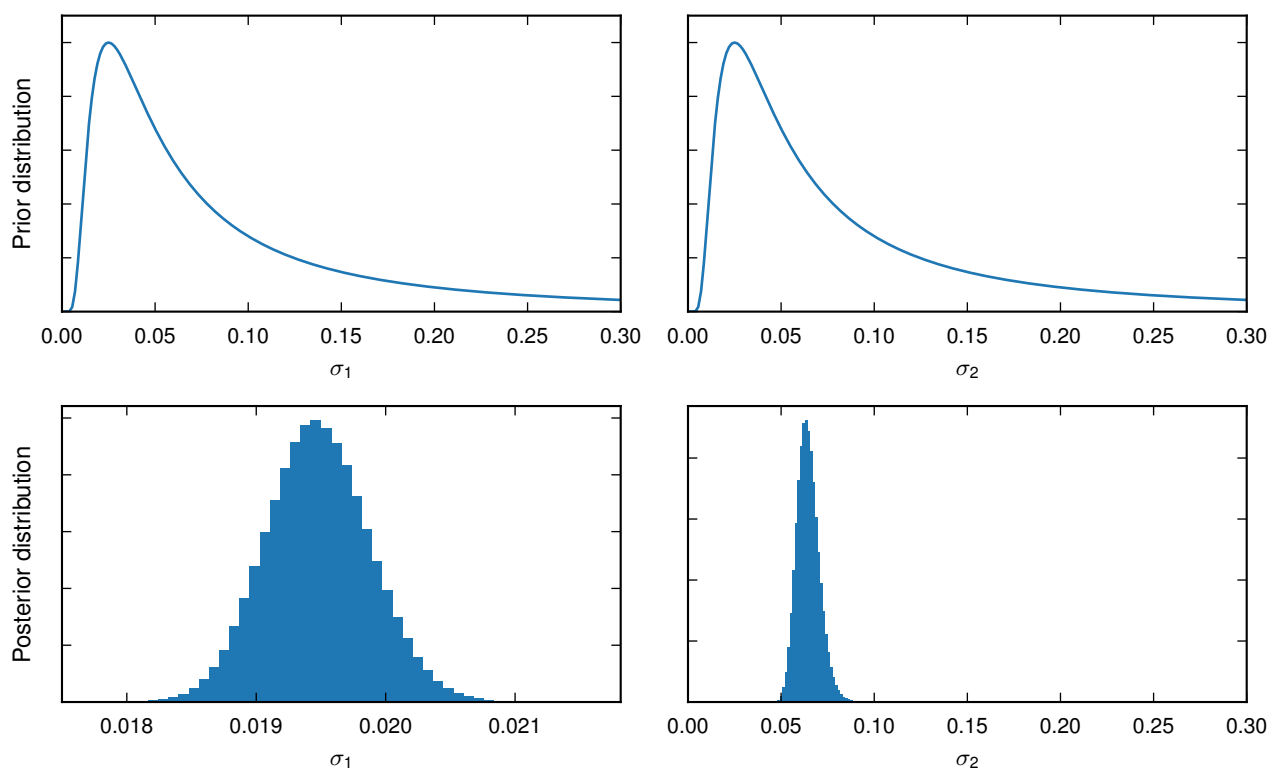


Figure S4: Prior distributions (top row) and posterior distributions (bottom row) for the hyper parameters σ_1 (left column) and σ_2 (right column). The parameter σ_1 is defined by assuming that the errors, defined as the difference between the DFT energy and the CE energy, are normally distributed with zero mean and variance σ_1^2 . The posterior distribution for σ_1 thus indicates the magnitude of the error in the model, but note that σ_1 relates to errors after weighting according to Au concentration and the real error is therefore smaller than what σ_1 indicates. The parameter σ_2 is defined as the variance of the normally distributed prior for the ECIs.

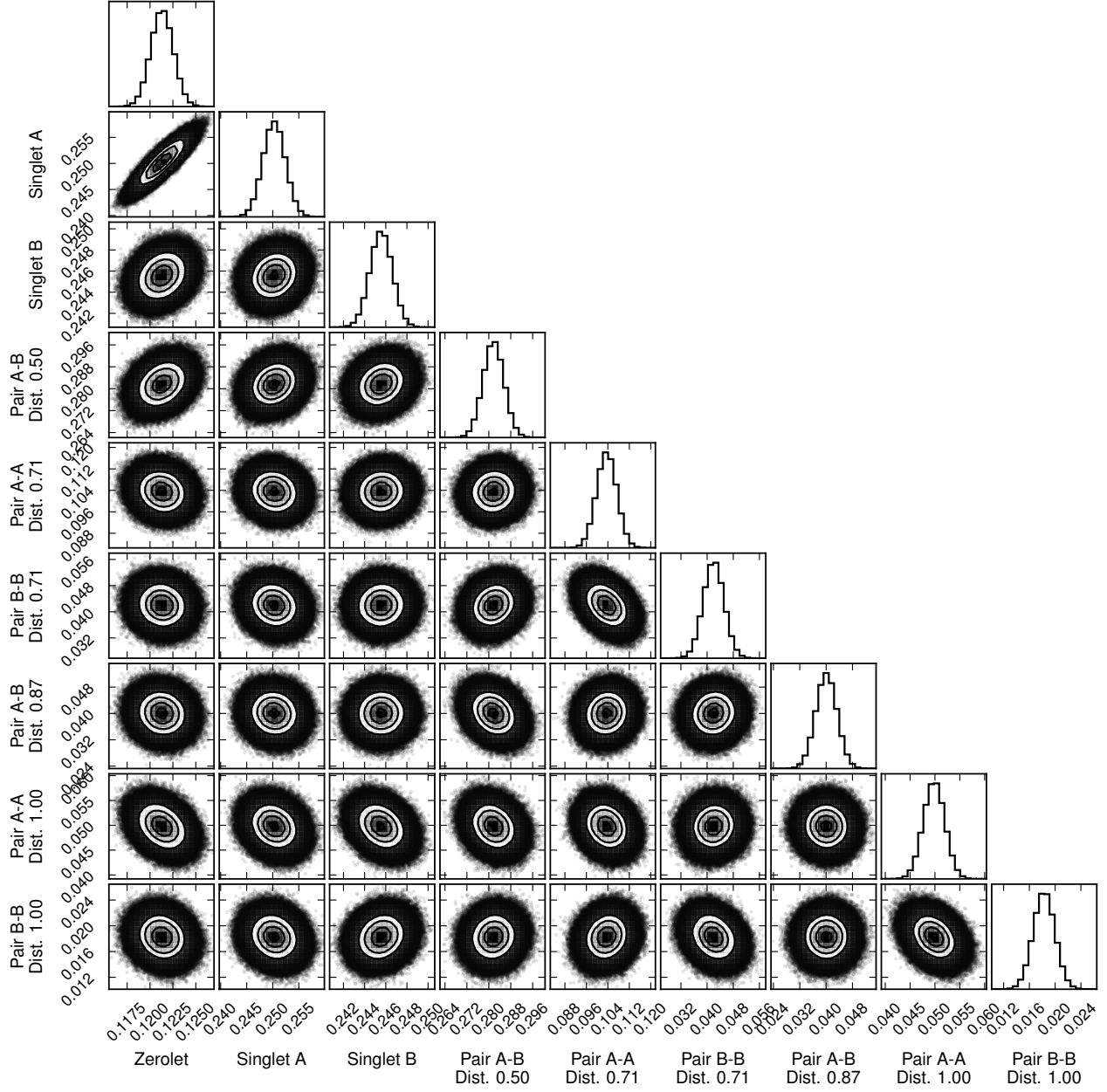


Figure S5: Corner plot (24) for the 9 most short-ranged ECIs (in units of eV/formula unit), showing the posterior distribution for each ECI (plots on the diagonal) as well as the correlation between each pair of ECIs. A and B in the labels refer, respectively, to the Pd–Au and H–vacancy sublattices. For example, A–A means that the ECI describes an energy related to the interaction between Au/Pd and Au/Pd. The labels also specify the distance between the atoms in each pair in units of the lattice parameter.

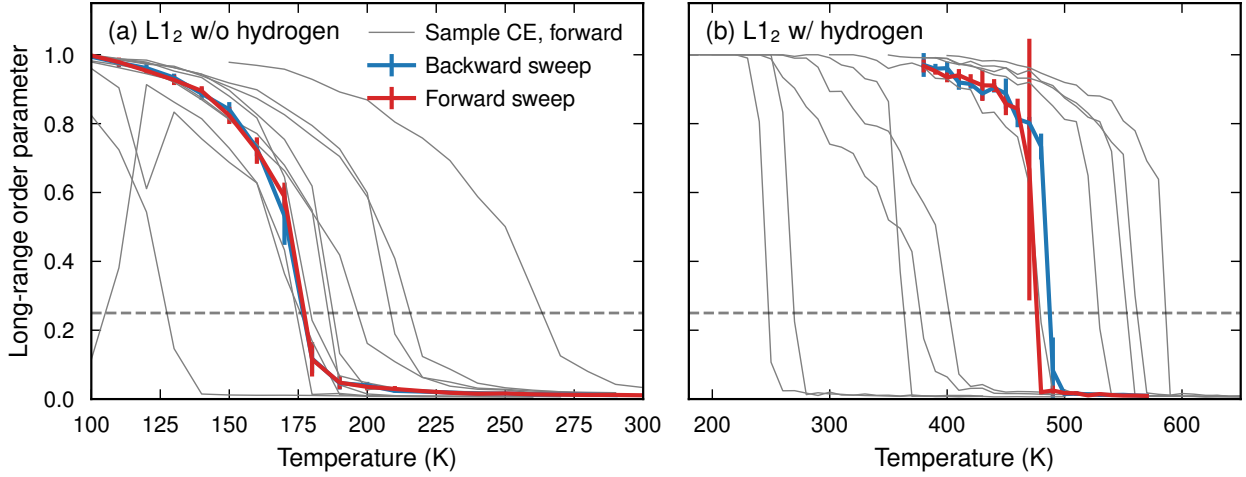


Figure S6: Estimation of critical temperature for the L_{12} phase without hydrogen (a) and with 25% hydrogen (b). For these calculations, MC simulations were run in the canonical ensemble on the Pd–Au sublattice in (a) and on both sublattices in (b). The simulations were commenced from either the perfectly ordered phase and low temperature or a solid solution and high temperature, and the temperature was then, respectively, increased (“forward”) or decreased (“backward”), in steps of 10 K using 500 MC sweeps at each temperature. This was done with the CE developed in this work (red and blue lines) as well as with ten sampled CEs (grey lines, only forward sweep shown). LRO was quantified by the structure factor $S(\mathbf{q})$ (see main paper) using the maximum value of the three symmetrically equivalent versions of $\mathbf{q} = 2\pi/a_0(1, 0, 0)$, and normalized such that perfect order means order parameter equals 1. The critical temperature was estimated as the average of the temperatures where the forward and backward sweep reached 25% of maximum LRO. For a few of the sample CEs, the critical temperature in the hydrogen-free case was too low to be reliably sampled with this method, and the lines are discontinuous at low temperatures.

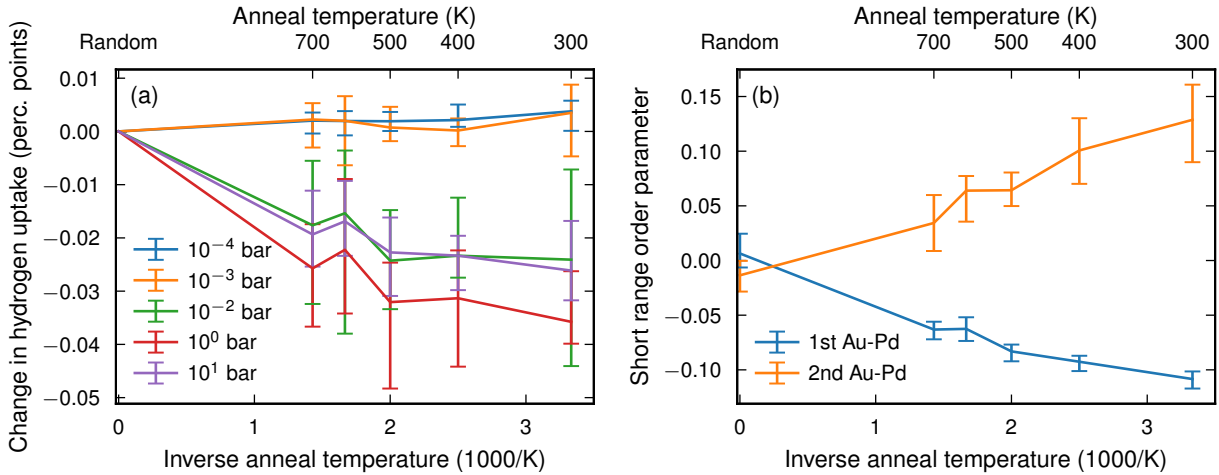


Figure S7: Change in uptake of hydrogen (a) at 300 K for Pd–Au with 25% Au as equilibrated at different temperatures (without hydrogen). The change in uptake depends on the loading pressure of H_2 , as is the strongest at approximately 1 bar (red line). The difference between the Pd–Au structures after annealing in different temperatures can be quantified by the SRO parameter (b) for the first (blue line) and second (orange) nearest-neighbor Pd–Au pair. The data was generated by a hydrogen-free simulation in the canonical ensemble at the respective temperature, and five snapshots were randomly selected from those trajectories. These Pd–Au structure of these snapshots was then frozen, and subjected to a simulation in the SGC ensemble on the H–vacancy sublattice, using chemical potential corresponding to the pressures specified in the legend in (a). Error bars indicate the spread over the five different structures, lines their average.

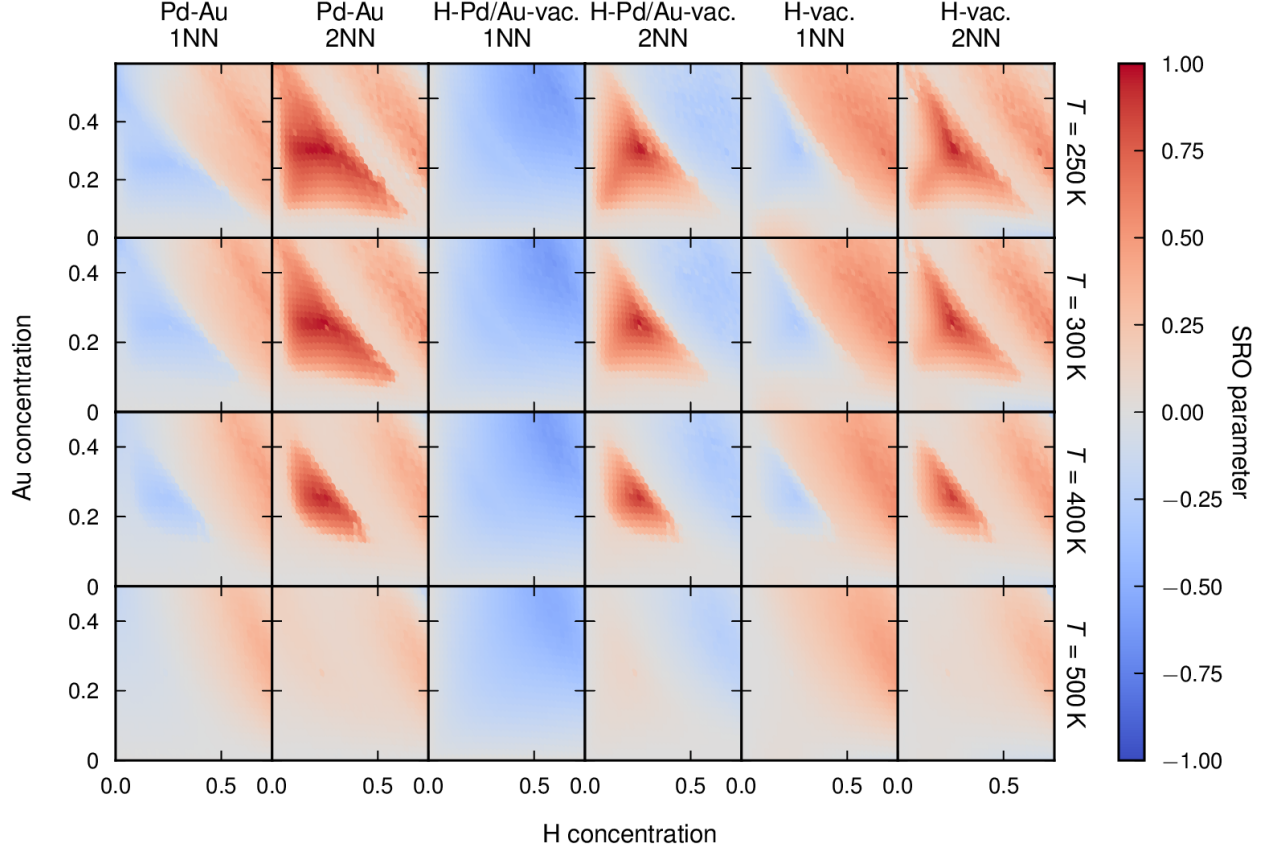


Figure S8: Short-range order (SRO) in full equilibrium as obtained with VCSGC-MC simulations at 250 K (top row), 300 K (second row), 400 K (third row), and 500 K (bottom row). Note that while this plot represents a single-phase region everywhere, the phase diagram predicts that in some regions, we expect phase separation. The ordered $L1_2$ phase is typically not clearly exhibited in the first nearest neighbor (1NN) shell. While this may appear unexpected in particular for the 1NN H-Pd/Au-vac. pair SRO, given that the ordered phase has hydrogen surrounded by Pd only, this is an effect of the fact that vacancies are included in the SRO, and they have a mix of Pd and Au nearest neighbors. Instead, the perfectly ordered phase correspond to $SRO = 1$ in the second shell in all three sublattices (vacancies have only Pd and Pd have only Au next nearest neighbors, for example). Further note that in several cases (1 NN Pd-Au, 2 NN H-vacancy, 1 NN H-vacancy), the SRO changes sign when the high-pressure (upper right half) region is entered.

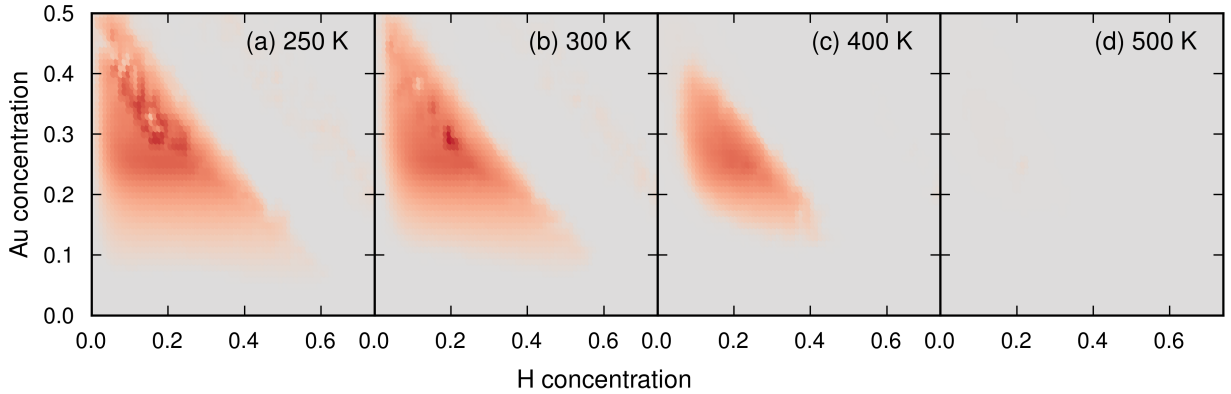


Figure S9: LRO parameter in full equilibrium at 250 K (a), 300 K (a), 400 K (a), and 500 K (d), quantified by the structure factor $S(\mathbf{q})$ (see main paper) using the maximum value of the three symmetrically equivalent versions of $\mathbf{q} = 2\pi/a_0(1, 0, 0)$. Red color indicates more order, gray color is complete lack of order.

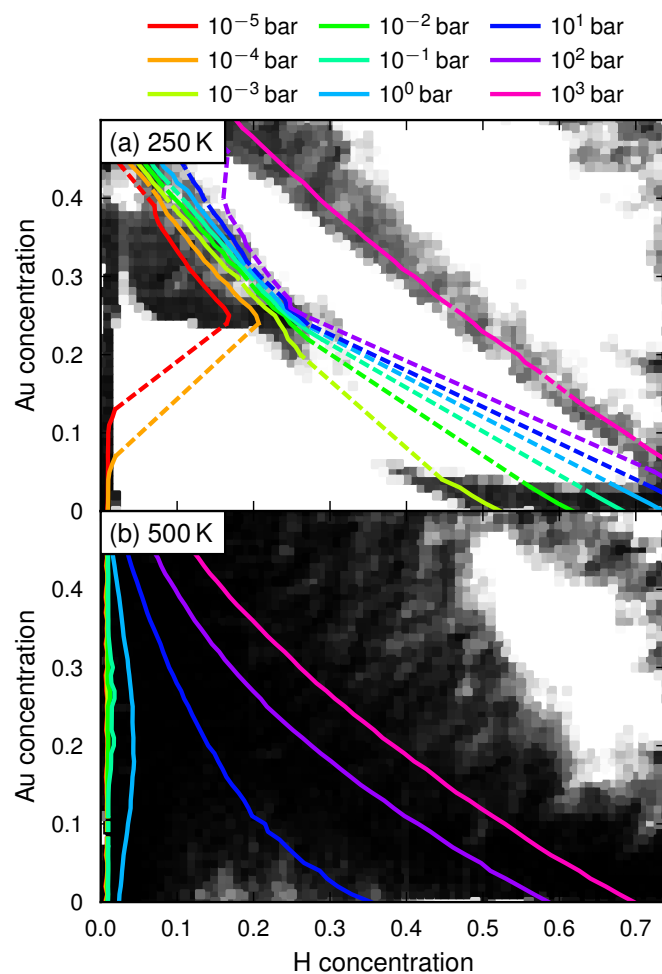


Figure S10: Phase diagram in equilibrium at 250 K (a) and 500 K (b).

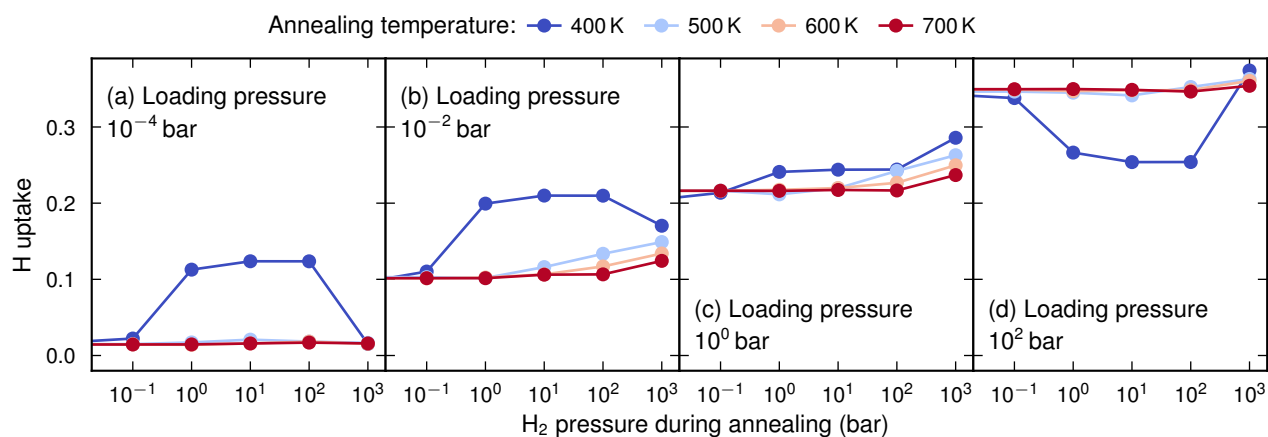


Figure S11: Hydrogen uptake at 300 K and H_2 pressure 10^{-4} bar (a), 10^{-2} bar (b), 1 bar (c), and 100 bar (d), in Pd–Au with 25% Au annealed at different temperatures (corresponding to different lines) and at different H_2 pressures (the abscissa). When annealing in 400 K (dark blue lines), the $L1_2$ phase forms at H_2 pressures between 1 and 100 bar, and this phase absorbs a significantly larger amount of hydrogen at 300 K and low pressures (a–b), whereas at high pressures it absorbs less than the solid solution Pd–Au (d). Very high H_2 pressures during annealing (at least 10 bar) are required to make a significant change to the hydrogen uptake if this ordered phase does not form.

References

- [1] M. Ångqvist, W. A. Muñoz, J. M. Rahm, E. Fransson, C. Durniak, P. Rozyczko, T. H. Rod, and P. Erhart, *ICET – A Python Library for Constructing and Sampling Alloy Cluster Expansions*, *Advanced Theory and Simulations* **2**, 1900015 (2019). doi:10.1002/adts.201900015.
- [2] G. L. W. Hart and R. W. Forcade, *Algorithm for generating derivative structures*, *Physical Review B* **77**, 224115 (2008). doi:10.1103/PhysRevB.77.224115.
- [3] G. Kresse and J. Furthmüller, *Efficiency of ab-initio total energy calculations for metals and semiconductors using a plane-wave basis set*, *Computational Materials Science* **6**, 15 (1996). doi:10.1016/0927-0256(96)00008-0.
- [4] G. Kresse and D. Joubert, *From ultrasoft pseudopotentials to the projector augmented-wave method*, *Physical Review B* **59**, 1758 (1999). doi:10.1103/PhysRevB.59.1758.
- [5] M. Dion, H. Rydberg, E. Schröder, D. C. Langreth, and B. I. Lundqvist, *Van der Waals Density Functional for General Geometries*, *Phys. Rev. Lett.* **92**, 246401 (2004). doi:10.1103/PhysRevLett.92.246401.
- [6] K. Berland and P. Hyldgaard, *Exchange functional that tests the robustness of the plasmon description of the van der Waals density functional*, *Physical Review B* **89**, 035412 (2014). doi:10.1103/PhysRevB.89.035412.
- [7] J. Sanchez, F. Ducastelle, and D. Gratias, *Generalized cluster description of multicomponent systems*, *Physica A: Statistical Mechanics and its Applications* **128**, 334 (1984). doi:https://doi.org/10.1016/0378-4371(84)90096-7.
- [8] J. Zhang, X. Liu, S. Bi, J. Yin, G. Zhang, and M. Eisenbach, *Robust data-driven approach for predicting the configurational energy of high entropy alloys*, *Materials & Design* **185**, 108247 (2020). doi:10.1016/j.matdes.2019.108247.
- [9] T. Mueller and G. Ceder, *Bayesian approach to cluster expansions*, *Physical Review B* **80**, 024103 (2009). doi:10.1103/PhysRevB.80.024103.
- [10] D. Foreman-Mackey, D. W. Hogg, D. Lang, and J. Goodman, *emcee: The MCMC Hammer*, *Publications of the Astronomical Society of the Pacific* **125**, 306 (2013). doi:10.1086/670067.
- [11] A. H. Nguyen, C. W. Rosenbrock, C. S. Reese, and G. L. W. Hart, *Robustness of the cluster expansion: Assessing the roles of relaxation and numerical error*, *Physical Review B* **96**, 014107 (2017). doi:10.1103/PhysRevB.96.014107.
- [12] M. Rahm, R. Hoffmann, and N. W. Ashcroft, *Ternary Gold Hydrides: Routes to Stable and Potentially Superconducting Compounds*, *Journal of the American Chemical Society* **139**, 8740 (2017). doi:10.1021/jacs.7b04456.
- [13] C. Donnerer, T. Scheler, and E. Gregoryanz, *High-pressure synthesis of noble metal hydrides*, *The Journal of Chemical Physics* **138**, 134507 (2013). doi:10.1063/1.4798640.
- [14] M. A. Biot, *Mechanics of incremental deformation* (New York: Wiley, 1965).
- [15] B. Sadigh and P. Erhart, *Calculation of excess free energies of precipitates via direct thermodynamic integration across phase boundaries*, *Physical Review B* **86**, 134204 (2012). doi:10.1103/PhysRevB.86.134204.
- [16] B. Sadigh, P. Erhart, A. Stukowski, A. Caro, E. Martinez, and L. Zepeda-Ruiz, *Scalable parallel Monte Carlo algorithm for atomistic simulations of precipitation in alloys*, *Physical Review B* **85**, 184203 (2012). doi:10.1103/PhysRevB.85.184203.
- [17] R. Schwarz and A. Khachaturyan, *Thermodynamics of open two-phase systems with coherent interfaces: Application to metal-hydrogen systems*, *Acta Materialia* **54**, 313 (2006). doi:10.1016/j.actamat.2005.08.044.
- [18] R. B. Schwarz, A. K. Khachaturyan, A. Caro, M. I. Baskes, and E. Martinez, *Coherent phase decomposition in the Pd-H system*, *Journal of Materials Science* **55**, 4864 (2020). doi:10.1007/s10853-019-04179-z.
- [19] H. Frieske and E. Wicke, *Magnetic Susceptibility and Equilibrium Diagram of PdH_n*, *Berichte der Bunsengesellschaft für physikalische Chemie* **77**, 48 (1973). doi:10.1002/bbpc.19730770112.

- [20] R. Lässer and K. H. Klatt, *Solubility of hydrogen isotopes in palladium*, Physical Review B **28**, 748 (1983). doi:[10.1103/PhysRevB.28.748](https://doi.org/10.1103/PhysRevB.28.748).
- [21] C. Picard, O. J. Kleppa, and G. Boureau, *A thermodynamic study of the palladium–hydrogen system at 245–352°C and at pressures up to 34 atm*, The Journal of Chemical Physics **69**, 5549 (1978). doi:[10.1063/1.436550](https://doi.org/10.1063/1.436550).
- [22] R. Bardhan, L. O. Hedges, C. L. Pint, A. Javey, S. Whitelam, and J. J. Urban, *Uncovering the intrinsic size dependence of hydriding phase transformations in nanocrystals*, Nature Materials **12**, 905 (2013). doi:[10.1038/nmat3716](https://doi.org/10.1038/nmat3716).
- [23] T. B. Flanagan and D. Wang, *Low temperature hydrogen and deuterium isotherms for Pd and some of its binary alloys*, Journal of Alloys and Compounds , 157434 (2020). doi:[10.1016/j.jallcom.2020.157434](https://doi.org/10.1016/j.jallcom.2020.157434).
- [24] D. Foreman-Mackey, *corner.py: Scatterplot matrices in Python*, The Journal of Open Source Software **1**, 24 (2016). doi:[10.21105/joss.00024](https://doi.org/10.21105/joss.00024).